

AD-A219 391

STUDIES OF SEA ICE THICKNESS AND CHARACTERISTICS  
FROM AN ARCTIC SUBMARINE CRUISE  
Phase III

Final Report on Phase III work accomplished under  
Contract N00014-89-C-0014 between  
October 1 1988 and September 30 1989

DTIC  
S ELECTE D  
MAR 19 1990  
D CS

SAIC Polar Oceans Associates  
Block A2, Westbrook Centre  
Milton Road  
Cambridge CB4 1YQ

February 26, 1990

DISTRIBUTION STATEMENT A

Approved for public release  
Distribution Unlimited

90 03 08 017

## 1. INTRODUCTION

This report is a summary of achievements during Phase III of Contract N00014-89-C-0014 and a reduced version of the progress report issued at the end of summer 1989. The latest versions of two submitted papers are included as appendices.

SAIC is indebted to representatives of the funding agencies for valuable comments made during and since the progress meeting held in Washington in September 1989. While no further technical effort under Phase III has occurred since that meeting, the emphasis of this report reflects that interaction.

Phase III work was co-ordinated by Dr P Wadhams, working out of SAIC Polar Oceans Associates Division, Cambridge UK. NASA's chief investigator was Dr J Comiso (Goddard).

Project Team responsibilities were initially as follows:

Co-ordinator	Dr Wadhams, SAIC/SPRI
NASA Principal Investigator	Dr Comiso, Goddard
Submarine Data	Dr Wadhams, SAIC
Passive Microwave	Dr Comiso, Goddard
AOL	Dr Tucker, CRREL
Co-location of data sets	Dr Krabil & Swift, Wallops; and Dr Crawford, JPL

Throughout the Fiscal Year 1989, project team responsibilities evolved in response to immediate needs for data dissemination or analysis. In November 1988, a project workshop was held in Cambridge to discuss and agree data analysis effort and responsibilities. In December 1988 Wadhams, Comiso and Crawford met at the AGU Fall Meeting in San Francisco to review progress. A third workshop was held at NASA Wallops on 27-28 March 1989 (Wadhams, Comiso, Krabil, Swift, Tucker and Crawford attending).

At these meetings, two papers were planned as Phase III deliverables. The first paper (Wadhams *et al.* 1989) was submitted during summer 1989, for publication in International Journal of Remote Sensing. The second paper (Comiso *et al.* 1989) was completed during autumn 1989 and submitted to the Journal of Geophysical Research at the end of the year. The papers are included in the report in Appendices I and II, respectively.

## 2. BACKGROUND

In May 1987 a collaborative experiment took place in the Arctic Ocean. A British submarine and two remote sensing aircraft co-operated in concurrent profiling and imaging of the upper and lower sea ice surfaces along the same track.

The submarine was equipped with a 780 Upward-looking Sonar System (narrow beam, 48 kHz), feeding chart and digital recorders, and an

EDO Western 602 Sidescan Sonar towfish (100 kHz) feeding an EDO 706 sidescan mapping system.

The two remote sensing aircraft comprised:

A. A NASA P-3A equipped with:

- i Advanced Multichannel Microwave Radiometer (AMMR) with 37GHz and 18GHz dual polarised channels and 21GHz vertically polarised channel,
- ii Electrically Scanning Microwave Radiometer (ESMR) operating at 19GHz,
- iii Airborne Oceanographic Lidar (AOL),
- iv PRT-5 infra-red radiometer,
- v aerial cameras and video;

B. A Cessna Conquest equipped with:

- i the Intera STAR-2 X-band HH-polarised synthetic aperture radar (SAR), giving a 63km swath width.

The SAR mission was funded by the UK Admiralty Research Establishment.

The experiment provided opportunities for validation of remote sensing systems using ice of known type and thickness. During Phase III datasets were analysed by SAIC Polar Oceans Associates (submarine and SAR data), NASA Goddard and Wallops (P-3A data) and NASA JPL (aerial photography and SAR registration).

### 3. PHASE III SUMMARY

#### 3.1 Main Thrusts of Phase III Work

- 3.1.1 Technical decisions made at Project Meetings and by telemail communication
- 3.1.2 Registration and co-location of data sets
  - 3.1.2.1 Subset of 'away from Pole' high Arctic data
- 3.1.3 Statistical analysis of individual data sets
- 3.1.4 Comparative analysis of data sets

STATEMENT "A" per Tom Curtin  
ONR/Code 1125AR  
TELECON

3/19/90

CG



per call

Page	
Date	
Dist	
A-1	

### 3.2 Methodology

- 3.2.1 Generation of 780 Upward-looking sonar statistics
- 3.2.2 Selection of location for initial multisensor analysis
- 3.2.3 For selected region worthy of intensive study
  - 3.2.3.1 Co-registration of several data sets
  - 3.2.3.2 Individual analyses
  - 3.2.3.3 Multivariate analyses

### 3.3 Data Sets

- 3.3.1 Submarine
  - 3.3.1.1 780 Narrow Beam Upward-looking Sonar
  - 3.3.1.2 EDO Sidescan Sonar
- 3.3.2 NASA P-3A
  - 3.3.2.1 Airborne Oceanographic Lidar (AOL)
  - 3.3.2.2 Advanced Multichannel Microwave Radiometer (AMMR)
  - 3.3.2.3 Electrically Scanning Microwave Radiometer (ESMR)
  - 3.3.2.4 PRT-5 Infrared Radiometer
  - 3.3.2.5 Cameras and Video
  - 3.3.2.6 GTS Position Fixing
- 3.3.3 Intera Cessna Conquest
  - 3.3.3.1 Intera Star 2 X-band Synthetic Aperture Radar

### 3.4 Data Availability

NB. No data were available for the exercise at the North Pole.

- 3.4.1 Submarine
  - 3.4.1.1 780
    - 3.4.1.1.1 3050km Away from Pole
      - 3.4.1.1.1.1 Statistics generated
    - 3.4.1.1.2 500km in MIZ
      - 3.4.1.1.2.1 ARE data set, not used in this program
    - 3.4.1.1.3 4600km to the pole
      - 3.4.1.1.3.1 No analysis of these 780 data has been undertaken.
  - 3.4.1.2 Sidescan Sonar
    - 3.4.1.2.1 Away from Pole data only

- 3.4.2 P-3A
  - 3.4.2.1 Matching submarine data, away from pole only
- 3.4.3 SAR
  - 3.4.3.1 Matching submarine data, away from Pole only
- 3.4.4 Combined data sets
  - 3.4.4.1 Detailed co-registration of all available data
    - 3.4.4.1.1 May 20th at approximately 85°N, length 200km
  - 3.4.4.2 Selected 'best fit' 60km section
    - 3.4.4.2.1 Section 16
  - 3.4.4.3 10km and larger 20km subsections selected

### 3.5 Table of Data Status

- \* ~10km subsection for the first multisensor analysis was expanded in spring 1989 to ~20km.

Data Set	Lengths - Registered Data	Analysis State
780	4600km to Pole 3050km away from Pole (Sections 1 to 68)	Not analysed Analysed
of which -	60km for AOL comparison * ~10km for multisensor work	Analysed Analysed
	500km away from Pole	ARE data
Sidescan	3050km away from Pole	Viewed
of which -	60km for AOL comparison * ~10km for multisensor work	Feature Match Analysed
	500km away from Pole	ARE data
SAR	150km away from Pole	Feature Match
of which -	* ~10km for multisensor work	Analysed
AOL	134km away from Pole	
of which -	60km for 780 comparison * ~10km for multisensor work	Analysed Plotted
AMMR	Exact total length unknown	
of which -	150km away from Pole 70km for ice type work * ~10km for multisensor work	Analysed(SAR) Analysed Plotted
ESMR	Exact total length unknown	
of which -	* ~10km x 2 for multisensor	Plotted
Other Data	Exact total lengths unknown	Viewed

### 3.6 Phase III Data Analysis

3.6.1 3050km 780 Data, Sections 1 to 61 away from pole

3.6.2 Multisensor Analysis for a selected 50km section. This section was selected for detailed comparison before and during the meeting in Cambridge, November 1988

3.6.2.1 Clear positioning of the submarine on available SAR imagery was required

3.6.2.2 The submarine had to be travelling at a constant speed

3.6.2.3 Mainly good quality SAR data were available, together with good quality sidescan data. Data were available from all other sensors for the section

3.6.2.4 SAIC's prime task was locating the submarine by feature matching the SAR/780 with concurrent sidescan data

3.6.2.5 Comparisons of submarine/aircraft data were **only possible** by using sidescan data.

3.6.3 A selected subsection within Section 16 (selected at the Cambridge meeting, November 1988)

3.6.3.1 This subsection is approximately 10km long. It was chosen because:

3.6.3.1.1 In it, the P-3A track was very close to the submarine track.

3.6.3.1.2 Several prominent ice features and narrow leads were visible on the SAR, that could be matched on sidescan, 780, AMMR, ESMR and AOL.

3.6.3.1.3 One wide lead was the most conspicuous feature.

### 3.7 Phase III Objectives

#### 3.7.1 Coarse data registration

#### 3.7.2 Selection of records For detailed analysis

##### 3.7.2.1 Section 16

##### 3.7.2.1.1 10km sub-section

#### 3.7.3 Fine scale data registration

#### 3.7.4 Technical liaison to define analysis methods

#### 3.7.5 Analyses of individual data sets

#### 3.7.6 Detailed multisensor analyses

#### 3.7.7 Production of project reports and publications

The primary objectives of the Phase III program have been accomplished.

### 3.8 Phase III Achievements

#### 3.8.1 Technical liaison between groups

#### 3.8.2 Selection of analysis sections

#### 3.8.3 Detailed data registration

#### 3.8.4 Significant single data set analysis

##### 3.8.4.1 780

##### 3.8.4.1.1 Generation of Statistics (Sections 1-61)

##### 3.8.4.1.2 780 Wave Number Analysis

##### 3.8.4.1.2.1 Early results output

##### 3.8.4.2 SAR

##### 3.8.4.2.1 Developing Methods for Image Analysis

##### 3.8.4.2.1.1 Image Segmentation

##### 3.8.4.2.1.2 Image Classification



### 3.8.5 Comparative analyses

#### 3.8.5.1 SAR with Sidescan

##### 3.8.5.1.1 Matched features, mainly visual analysis

#### 3.8.5.2 SAR with 780

##### 3.8.5.2.1 Matched features and proven correlations

##### 3.8.5.2.2 Determined optimal averaging window

#### 3.8.5.3 SAR with AOL

##### 3.8.5.3.1 Matched features and proven correlations

#### 3.8.5.4 780 with AOL

##### 3.8.5.4.1 Comparison of statistics

##### 3.8.5.4.2 Confirmed ice draught / elevation relation

##### 3.8.5.4.3 Investigating sail / keel relationship

### 3.8.6 Preparation of publications

#### 3.8.6.1 Thus far, Phase III work is reported in two publications: Wadhams *et al.* 1989 and Comiso *et al.* 1989

### 3.8.7 Preparation of project reports

## 4. CO-REGISTRATION

The submarine spent ten days operating independently in the Arctic, collecting Upward-looking Sonar data and terminating at the North Pole. There followed 23 days of concurrent submarine and aircraft profiling, along a track running southward from the Pole towards Greenland, then eastward towards Fram Strait, with a final collaborative day in running southward through the East Greenland pack ice. During these periods the submarine and two aircraft navigated by Inertial Navigation System (INS), with additional position fixes from the Global Positioning System (GPS) on the P-3A for part of each day.

Registration of the submarine data involved conversion of the Upward-looking Sonar record from a function of time to a function of distance. This was accomplished using recorded position fixes

for the submarine, together with measured curves of acceleration and deceleration during times of speed change.

During Phase III detailed registration was undertaken for the aircraft, for a 200km section to the north of Greenland. GPS and high-altitude photography information were used to register the P-3A sensor data to SAR imagery. Features such as leads were matched between the data sets by a NASA team (Wadhams et al. 1989). In a similar manner, SAIC co-registered the submarine track with the SAR imagery, using the Sidescan Sonar record to match features with the SAR. This was attempted for approximately 60km within the 200km section. The SAR imagery became the base data set on which both the P-3A and submarine tracks were superimposed. Co-registration of data along one sample of track permitted systematic comparisons of sensor outputs to be carried out.

## 5. ANALYSIS OF SUBMARINE DATA

### 5.1 780 Upward-looking Sonar

Upward-looking Sonar profiles were obtained using the sonar with a transducer on the top of the submarine fin ( $10^\circ$  beamwidth). The effective footprint of the beam on the ice bottom was about 15m. Discussion of beamwidth problems and their solution is given in Wadhams (1981).

The raw digital data obtained were quality-controlled and gaps filled by manual digitisation of the chart record. Range was converted to draught by removing the profile of submarine depth variations. This was done by identifying points on the record (using the charts) that were considered to be definitely open water (very strong echoes, often containing multiple returns). These points were joined by a smooth polynomial, which was then subtracted from the range to leave a record of draught versus time. This record of draught versus time was converted to one of draught versus distance.

This was achieved using the hand-written submarine log in combination with the on-board Ships Inertial Navigation System (SINS) log. Finally, the record was quadratically interpolated to yield a quality-controlled discrete ice draught series at 1m along track intervals.

For this contract, the 1m ice draught record was analysed in 50km along track sections. The analysed record length is 2,500km (50 sections).

#### 5.1.1 Basic analyses of Upward-looking Sonar data

Various statistical analyses were undertaken for each 50km section. Line printer output and sample graphical results for a sample section (Section 1) were presented in the progress report, issued in September 1989, together with a commentary on each output statistic. Analyses were undertaken for the following parameters of the underice environment:

- A) the normalised probability distribution of ice draught, using a bin size of 0.1m. The total is 100,000. The ice draught distributions are then summed in 0.5m and 1m depth bins, in order to give a clearer indication of the frequency distribution. The following derived statistics were output, both with and without negative draughts set to zero:

- i modal draught
- ii mean draught
- iii root mean square (rms) draught
- iv variance
- v standard deviation
- vi median draught

- B) Polynya/lead distribution. A polynya or lead is defined as a continuous sequence of depth points, none of which exceed a value of 0.5m, 0.75m or 1m. These three criteria are used in order to distinguish between leads which are at different stages of re-freezing. The leads are classified not only by ice draught but also by along track lead width in 10m intervals up to 100m, then in 20m intervals up to 200m and 50m intervals up to 1000m. Two tables are output. One shows the number of leads per 100km. The other is of actual lead numbers encountered in the section. The following derived statistics were output for each of the depth criteria:

- i mean number of leads encountered per 100km
- ii mean lead width along track
- iii rms lead width along track
- iv variance of lead width

v     standard deviation of lead width  
vi    median lead width

These statistics are repeated, zeroing negative depth values. The results are identical, except for rounding errors.

Also, for each draught criterion, the normalised fraction of the total number of leads occurring in each width range is given.

- C) Smooth ice distribution. Smooth ice is defined as a continuous sequence of depth points, at least 10m in length, in which the bottom surface slope is always less than 0.05. (Rough ice does not meet this criterion.) For each 50km section, the percentage of the ice profile occupied by smooth ice is given, as is normalised frequency distribution of smooth ice draught (in 0.1m, 0.5m and 1m draught bins from -1 to 50m). These distributions reflect the preferred draughts reached by undeformed ice of varying ages. Young ice is usually less than 1m thick and first year ice less than 2m thick. The 10m minimum length criterion for sections of smooth ice safeguards against erroneous identification of pressure ridge crests and other turning points as being smooth ice.
- D) Rough ice distribution. Rough ice is defined as all ice that is not smooth ice. Thus, rough ice sections may be shorter than 10m. The same statistics are generated as for smooth ice.
- E) Smooth and rough ice length and draught analysis. A complete breakdown of each 50km record is provided, showing the length of each section of smooth ice and its mean draught, followed by the length and mean draught of the succeeding section of rough ice. The distribution of segment lengths and their mean draughts are given.
- F) Pressure ridge draught and spacing analysis. An independent pressure ridge is identified by a Rayleigh criterion algorithm. Each ridge in the record is listed with its draught and the spacing to the crest of the next ridge. Also, the number of pressure ridges in the record and the number per

100km are listed in 1m increments of draught. The following pressure ridge statistics are generated for ridges which are deeper than 5m and for ridges which are deeper than 9m.

- i number of pressure ridges in a record
- ii number per km of track
- iii mean draught
- iv rms draught
- v variance
- vi standard deviation
- vii median draught

Also output is the maximum pressure ridge draught in each 50km section and the number of ridges per 100km track. The probabilities and cumulative probabilities are shown for 20m categories of spacing up to 400m. This can indicate whether or not pressure ridge spacings in the central Arctic fit a lognormal distribution. Finally, various distributions (lognormal, negative exponential, logarithmic and exponential lognormal) are applied to the ridge spacing statistics and correlation coefficients calculated. In the case of MIZ ice, it appears that the negative exponential distribution usually offers a better fit than the lognormal.

The results of the analyses outlined above for Section 1 (starting at the North Pole) were issued by SAIC in the Summer 1989 progress report.

#### 5.1.2 Wave number spectra of Upward-looking Sonar data

An analysis was carried out for energy spectra of the underice surface. The wave number spectrum of the ice underside is of considerable importance. It is the basis of the method of small perturbations (MSP, a theoretical technique for estimating the sound scattering loss from the ice surface). It is also the basis of some theoretical approaches to the problem of internal wave generation under ice. Spectra were computed for each of the 50km sections.

Figure 1 shows the averaged spectrum of 38, 50km sections drawn from the high Arctic Ocean. Each underice record was sampled at 12m intervals. Underice records from the marginal ice zone region

typically show spectra where the energy density varies as  $k^{-3}$ . This is illustrated by Figure 2 (Guoliang and Wadhams 1989), which represents data collected on a 1985 submarine cruise. Figure 1 shows no such variation in the ice interior. Instead, the energy density appears to vary approximately as  $k^{-4}$  for wavelengths less than 11m and as  $k^{-2}$  or even  $k^{-1}$  at longer wavelengths. Thus, there is a 'knee' at about 11m wavelength, clearly seen in the averaged spectrum and also visible in most of the individual 50km sections (not shown). This appears to be unrelated to either the sonar beam diameter (8m or less) or any wavelength of platform porpoising.

The knee may be a genuine feature of ice bottom roughness, marking the wavelength where roughness due to individual ice blocks on the underside gives way to the roughness due to entire ice features such as ridges and floes. Explanation of why  $k^{-4}$  and  $k^{-2}$  or  $k^{-1}$  variations are not seen in the marginal ice zone may be sought in high Arctic processes which do not operate in the MIZ (for example,  $k^{-4}$  - large scale ridging processes and for  $k$  or  $k^{-1}$ , seasonal freeze-thaw cycles that may give rise to a 'hummocky' ice bottom, (Wadhams, 1988; Wadhams and Martin, 1989)).

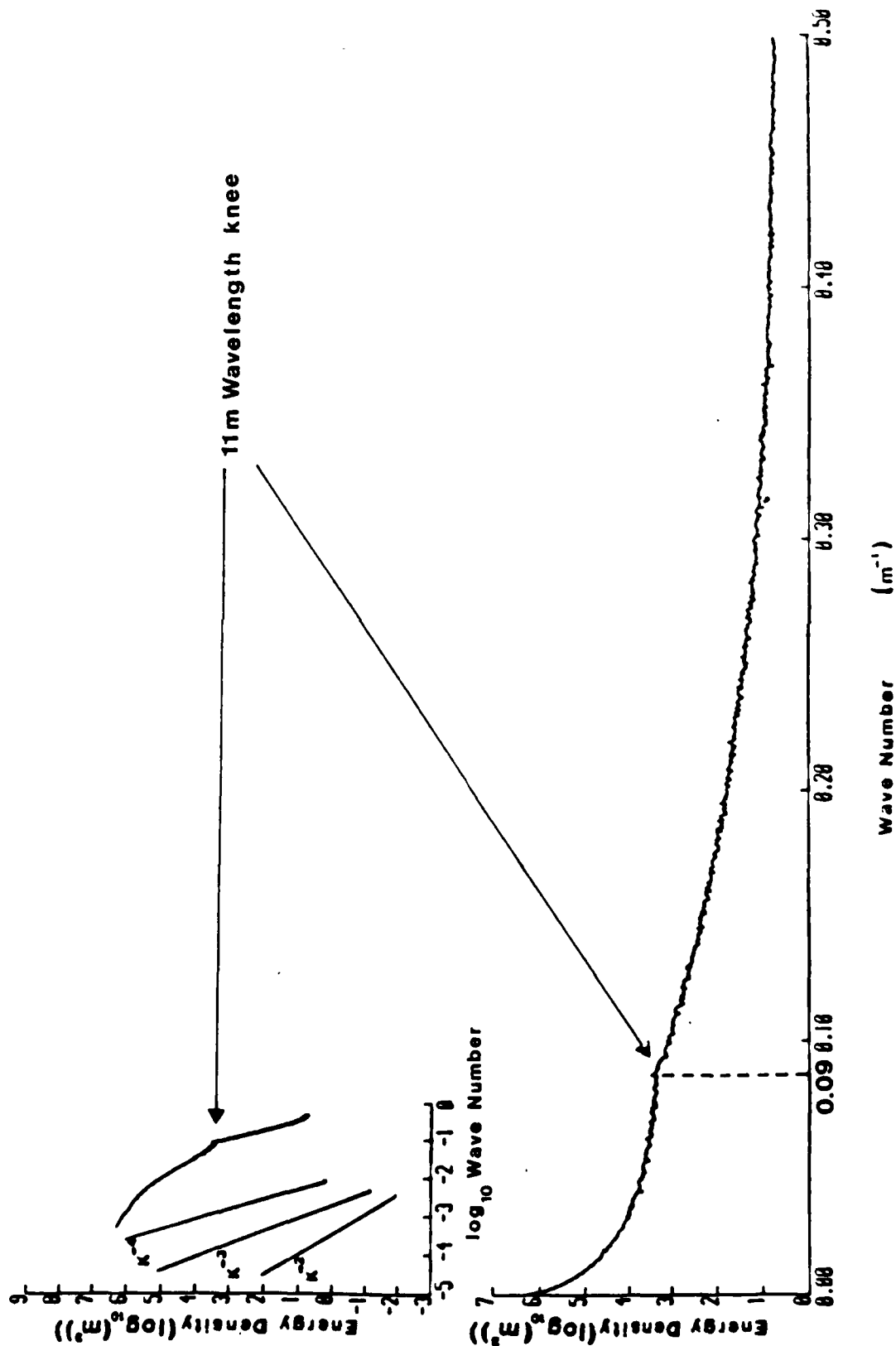


Figure 1. Mean wave number spectrum from 38 50km sections in central Arctic.  $K^{-2}$ ,  $K^{-3}$ ,  $K^{-4}$  decay lines are shown for comparison.

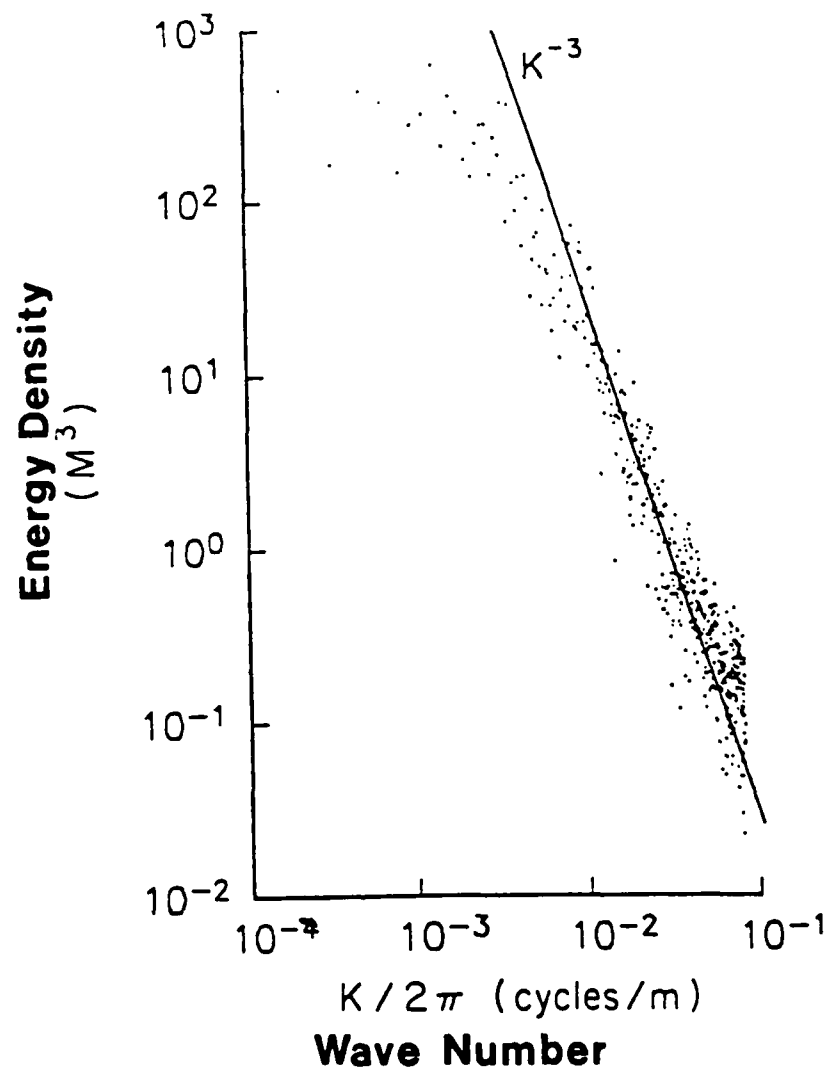


Figure 2. Wave number spectrum from the marginal ice zone in the Greenland Sea (from Guoliang and Wadhams, 1989).



By analysing further these valuable data, a description of the underice environment in wave number space should be forthcoming that is process-driven. This will provide a physical basis from which data analysis can continue that is geared to modelling and describing the underice environment acoustically.

## 5.2 Sidescan Sonar Analysis

Sidescan Sonar data were recorded on electrically sensitive paper, producing a fragile analogue record. Back-up recording was on analog magnetic tape which requires replaying through an EDO recorder. When the submarine was travelling at less than 8kts and kept constant depth, a geometrically correct chart record was generated (compensated for both depth and speed).

A total of 3000km of sidescan record was collected, of which only 1000km consisted of good quality data (i.e. geometrically correct), the remaining 2000km were of poor quality. After photocopying the dataset, various analyses were undertaken. Sidescan data were used in conjunction with SAR to register the datasets and with AMMR data to place the AMMR footprints on the SAR data in terms of underlying ice type. Also, comparative analyses were begun with Upward-looking Sonar data to obtain information concerning the true distributions of ridge slopes and lead widths.

## 6. SONAR/LASER COMPARITIVE ANALYSIS

As part of the intensive analysis reported in Comiso et al. (1989), a joint statistical analysis was carried out on three consecutive, corresponding 20km sections of ULS and laser data (Sections 1 to 3). Upward-looking Sonar statistics (Section 4.1) were compared with laser statistics (calculated in a similar fashion). An important result was obtained.

### 6.1 Comparison of Draught and Elevation Data

Analysis of the probability density functions (pdfs) was carried out for ice draught and elevation. The individual pdfs (Figure 3) show little variation between the three sections and no apparent association is observed between the two data distributions. The three sections were consecutive and were retrieved from almost

identical ice conditions (the heavily ridged zone north of Greenland). Thus, they were combined into a single 60km section.

The overall mean draught was compared with the overall mean elevation. The result was a ratio of 7.909. This ratio R should be related to mean ice and surface water densities  $\rho_i$  and  $\rho_w$  by:

$$R = \frac{\rho_i}{\rho_w + \rho_i} \quad (1)$$

Assuming a surface water density of  $1025 \text{ kg m}^{-3}$  (typical of Arctic surface water before melt begins), gives a mean ice density of  $910 \text{ kg m}^{-3}$ . This is comparable to the value found by Wadhams (1981) of  $915 \text{ kg m}^{-3}$ , using a similar method of draught/elevation comparison on Upward-looking Sonar and laser data.

Adjusting the horizontal scale of the elevation distribution (by expanding by a factor of 7.909) and the vertical scale (by compressing to yield the same area under the curve) results in Figure 4. Figure 4 shows a close agreement between draught and elevation pdfs. It would appear that surface features in the ice cover are magnified by a factor R on the underside. If a fraction F(h) of the ice cover has an elevation in the range h to (h+dh), then the same fraction F(h) will have a draught in the range 7.909h to 7.909(h+dh).

It is concluded that, in ice cover typical of the central Arctic, it is possible to derive the pdf of ice draught (and thus of ice thickness) solely from the results of airborne laser profiling. This result has important implications. Airborne surveys are easier to conduct than submarine surveys and our ability to monitor synoptically the ice thickness distribution in the Arctic will be greatly increased. This will be useful when seeking evidence of global change.

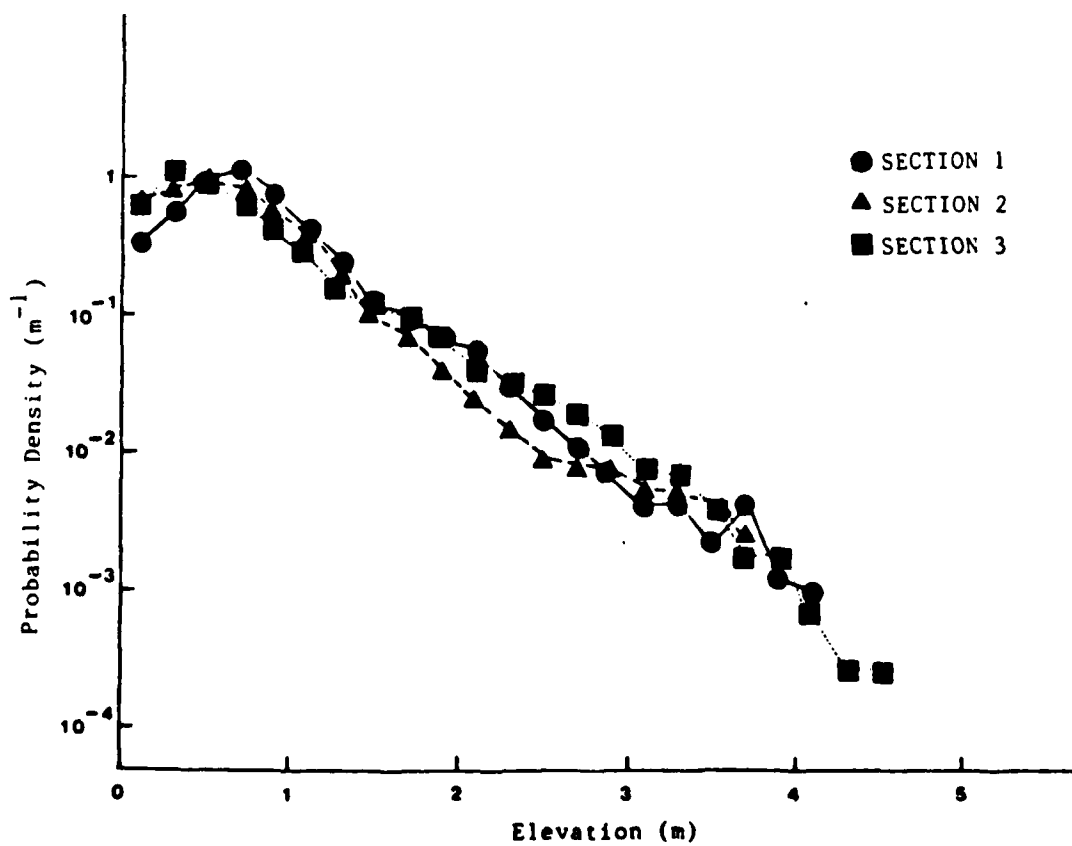
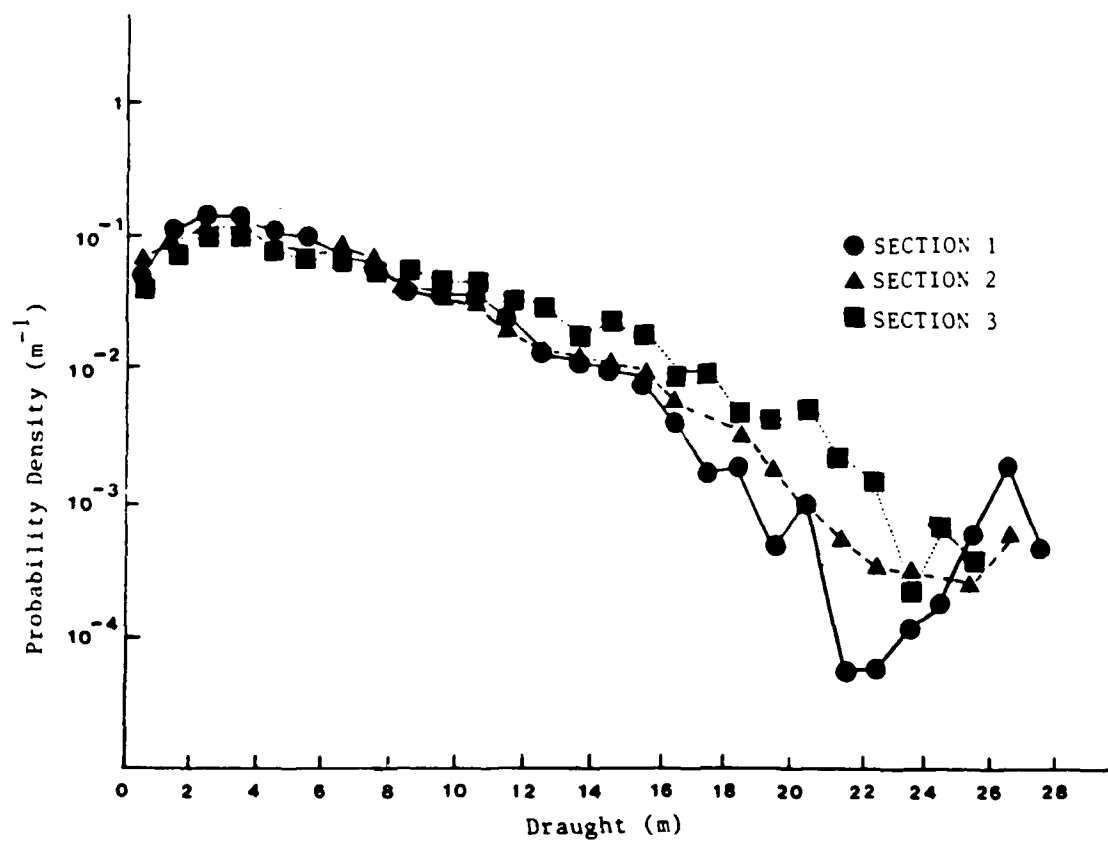


Figure 3. Distributions of the draught and elevations from 20km sections.

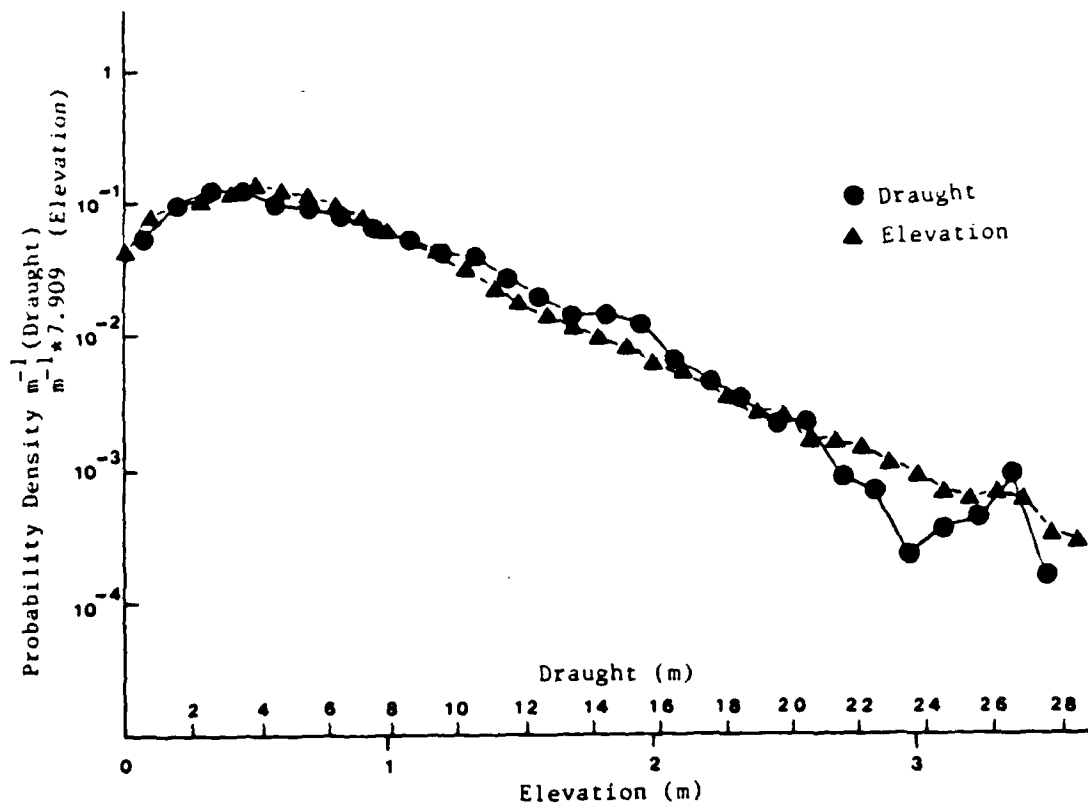


Figure 4. Results of a coordinate transformation in which the elevation distribution for 60km of track is stretched along the abscissa by a factor of 7.909 (mean draught / elevation ratio) and plotted against the corresponding draught distribution.

## 6.2 Comparison of Keels and Ridges

Using the three consecutive 20km sections discussed earlier, an analysis was also carried out of ridge and keel distributions. Figure 5 shows the three pairs of ridge elevation and draught distributions. All are approximately negatively exponential. By combining the sections and comparing the best fit negative exponentials, an empirical transformation could be carried out to derive keel distributions from sail distributions.

However, these transformations are not based on isostasy, as before. Each distribution takes the form:

$$n(h) dh = A e^{(-ah)} dh \quad (2)$$

where  $n(h)$  is the number density of ridges per unit distance and unit height increment. 'A' and 'a' are parameters characteristic of the ice regime. Using subscripts <sub>t</sub> and <sub>b</sub> for top and bottom surfaces, it was found that the use of the ratios  $a_b/a_t = 6.3$ ;  $A_b/A_t = 9.0$ , allows a keel distribution to be obtained from a ridge sail distribution. Again this requires testing using longer sections of data before it can be applied generally. These results are discussed fully in Comiso et al. (1989).

## 7. SONAR/LASER/SAR COMPARISONS

Two sections, respectively 10km and 22km in length were used to compare SAR brightness with ice draught and elevation (Wadhams et al. 1989). The original SAR pixels (15.45m x 5.6m) were subsampled 1 by 3 in order to obtain pixels covering an area of 15.45m x 16.8m (16.8m along track). The sonar and laser data were filtered to have equivalent along track resolutions. Point-for-point comparisons were then made of SAR brightness (on an uncalibrated linear scale of 0 to 255) and ice draught or elevation. To obtain valid regression analyses it was necessary to transform to square roots for SAR versus sonar and to square root (SAR) versus fourth root (laser). For the shorter 10km dataset it was found that the variances explained in transformed laser height and sonar depth by transformed SAR brightness were 15.8% and 17.1% respectively.

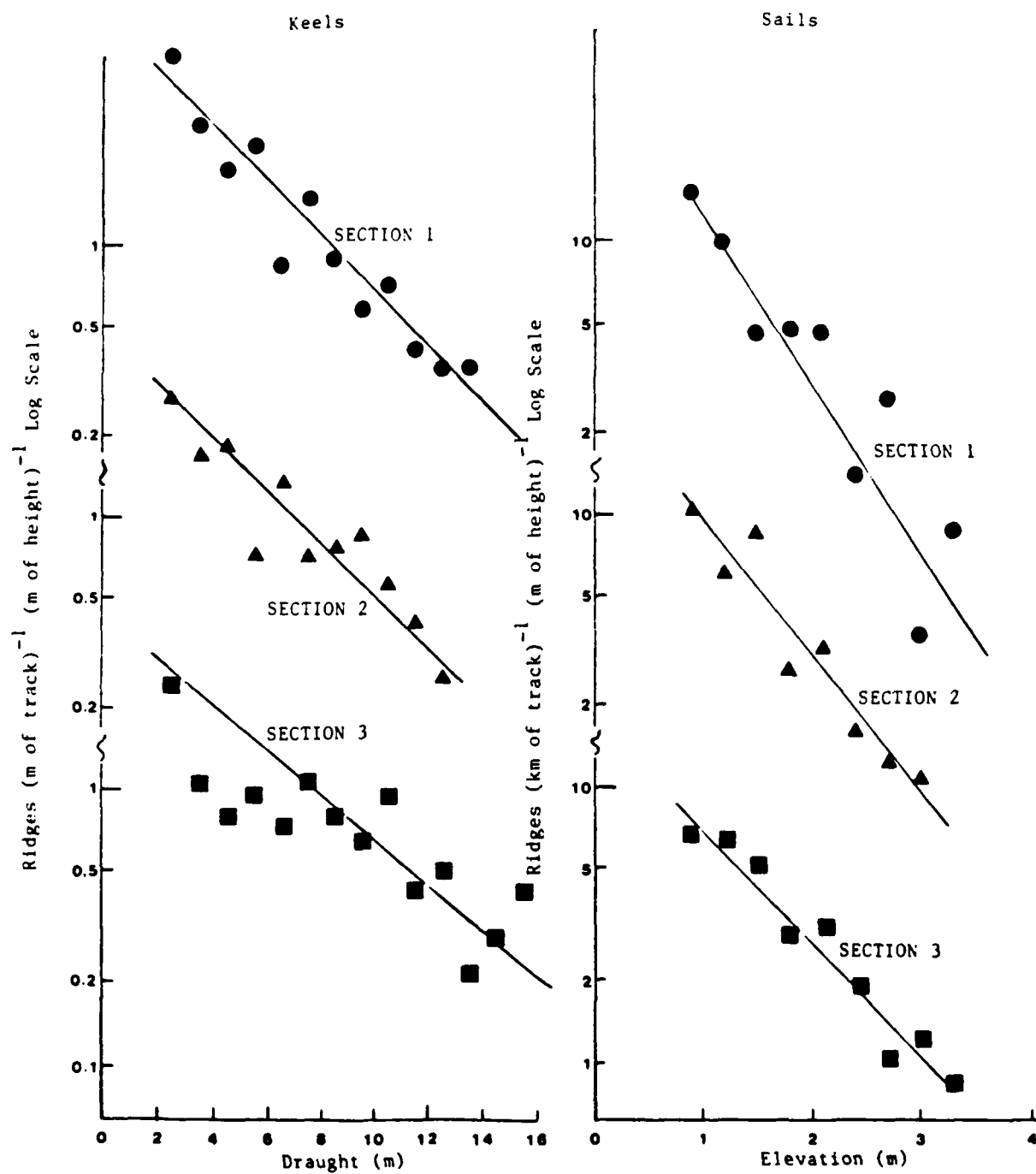


Figure 5. Distributions of keel draught and sail elevations for a 20km section.

The results were promising enough to justify a comparison for ice draught over the longer stretch of track. This allowed the determination of a suitable averaging length for SAR brightness and ice draught which would give the optimum correlation. It was found that using a 22km section required further speed adjustments in order to obtain a good SAR/sonar match and that it was not then necessary to use a square root transformation of the data. The resulting correlation coefficient for point-to-point comparison of sonar and SAR was 0.39. Both SAR and ice draught were then windowed over  $n$  pixels (i.e. along track distance of 16.8m) to try to improve the correlation.

The correlation coefficient  $r$  for SAR brightness versus ice draught increased with  $n$  but there is an upper useful limit dictated by the need to have a good spread of data in the scatter diagrams rather than closely clustered average ice data. It was found that  $n = 15$  gave the best windowed correlation, with an  $r$  of 0.68. This implies that 46% of the variance in ice draught can be explained in terms of SAR brightness variations. The corresponding averaging length is 252m, which is less than that required for the autocorrelation function of the ice bottom to go to zero (ie. each windowed data point corresponds to a reasonably coherent ice regime rather than averaged conditions).

The results give some promise that X-band SAR can be used as an empirical means of inferring ice draught distribution, or at least of inferring mean ice draught within a region. However, the correlation can never be as good as that between sonar and laser, since ice elevation and draught are connected by isostasy, whereas SAR brightness is determined by ice roughness, salt content and snow cover and is only indirectly related to ice draught.

#### **8. SONAR/PASSIVE MICROWAVE COMPARISONS**

The combination of platforms provides a unique opportunity for the validation of passive microwave data over long lengths of track. Initial analysis compared AMMR with ice type and ice draught. A co-registered track, 190km in length, was used as the test region. AMMR footprints were marked in their correct positions on the SAR image. When the P-3A was flown at low level, each footprint is an

approximate ellipse (along track length 33m and breadth 50m). The footprints were then transferred manually to a photomosaic of the sidescan sonar imagery, and the following analyses carried out:

- i dominant and subsidiary ice types within the footprint were determined by inspection of the sidescan image in conjunction with the SAR image. Ice was classified as ridged; undeformed multiyear; undeformed firstyear; young ice; refrozen lead; and open lead.
- ii where a footprint overlapped the submarine track itself, the ice draught was measured from the Upward-looking Sonar and given as an average for the 33m length of the footprint.

Some 280 footprints were analysed, of which 40 yielded ice draughts as well as types. Subsequently, these results have been used in further analyses by J. Comiso. Initial results are reported in Comiso et al. (1989). It was found that the large amount of deformed ice in this region hampered ice discrimination.

## **9. SAR DATA ANALYSIS**

An investigation was carried out on the SAR pixel frequency distribution for the various ice types. High Arctic multiyear ice could be separated visually into six distinct ice types. These were: lead; new ice; firstyear (FYR) ice; smooth floes; complex floes and ridges. Ice types within the above categories were confirmed by visual comparison of the SAR image with the sidescan data. This is seen as a preliminary analysis and it provides the basis for a two dimensional ice type analysis of Sidescan and SAR data, to derive a transfer function between the underice environment and the ice surface. This work is planned to proceed in the Fiscal Year 1990.

Briefly, the investigation determined whether or not different ice types within a SAR image of multiyear ice could be distinguished automatically using a digital thresholding procedure. First, the six ice categories were identified as training areas on the SAR image using the GEMS image processing system at SAIC. Once the ice types for the training areas were confirmed using the Sidescan, samples were taken across the entire image using SAR temperature



brightness values and texture to verify decisions made based on visual interpretation. For each ice type, several regions were selected for analysis within the study zone.

Pixel values were extracted from the SAR image for all the regions within the individual classes. Then the brightness values for each class were normalised and plotted as frequency histograms showing the pixel distribution for each ice category. The pixel frequency distributions for the six classes are shown on one graph (Figure 6). For each class basic statistics were calculated. The overlapping pixel frequency distributions for the six ice categories are clearly shown by Figure 6. Although they could be separated visually relatively easily, using tonal and texture information, the digital separation of the SAR pixel brightness distributions was too small.

Thus, four broader classes were defined. These were: lead and new ice; FYR ice; floe and complex floe (or multiyear ice, MYR) and ridges. these classes can be successfully separated digitally.

Investigation of class statistics can provide digital data on the textural properties of the ice types. Application of a simple maximum likelihood classification procedure, using the GEMS image analysis system, proved relatively successful, at least visually. Further investigation is required to develop more complex classification procedures for distinguishing ice types.

#### **10. PROGRAM STATUS**

The list of Phase III tasks in the contract scope of work was refined by the technical participants in the Cambridge Workshop of November 1988 and in the Wallops Workshop of March 1989. During Phase III the major effort was the processing and intercomparison of several data sets which were collected on May 20th 1987. These Phase III tasks were aimed at the production of scientific papers. Two submitted papers are delivered (see appendices).

The submitted papers satisfy the project requirements as outlined in the two workshop proceedings during the Fiscal Year 1989.

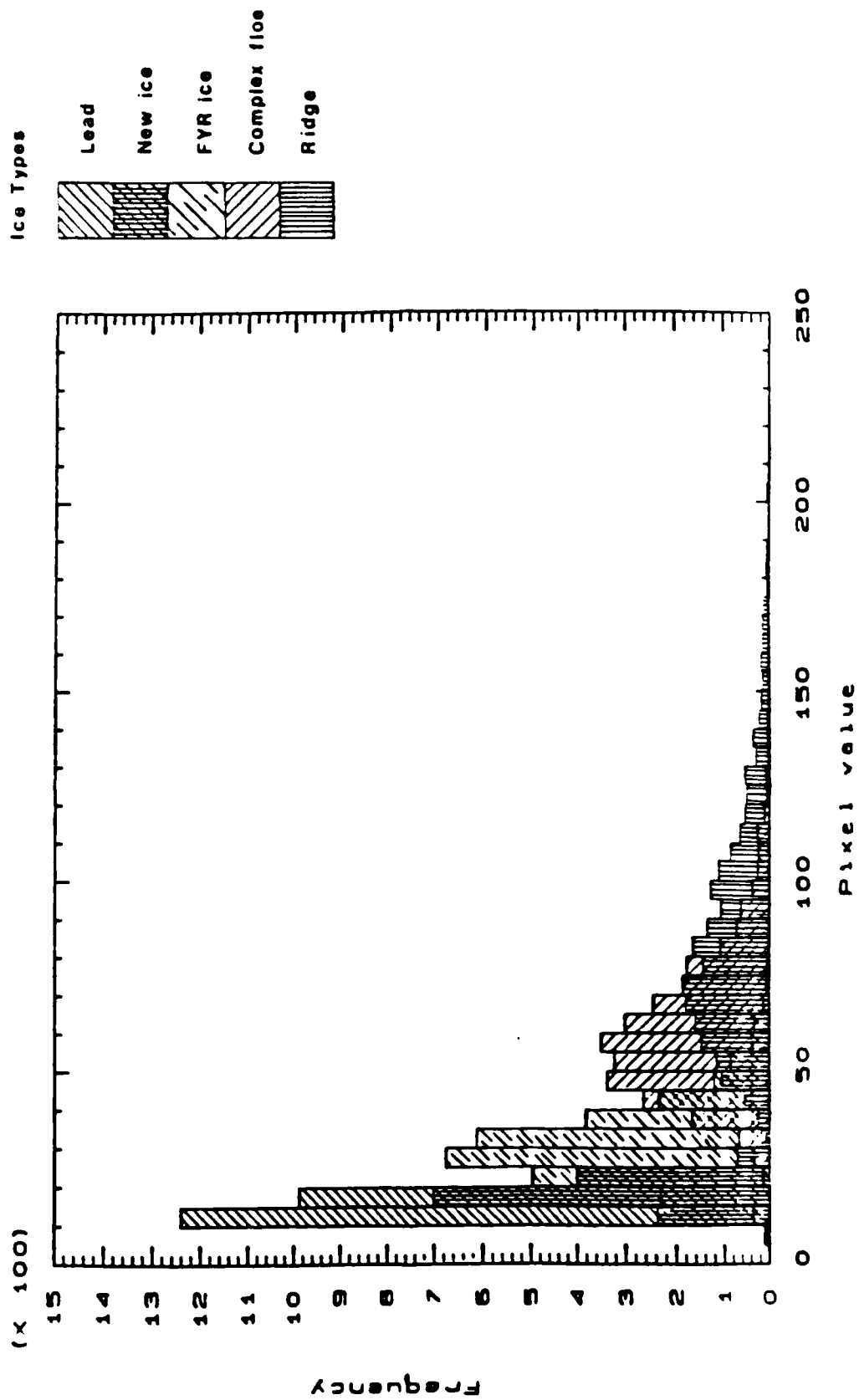


Figure 6. Histograms of SAR pixel frequency for five ice types based on training area analysis.

## 11. FISCAL YEAR 1990 EFFORT

Four lines of enquiry were suggested in the summer 1989 progress report. Following a progress meeting to discuss Phase III results, a change in emphasis was agreed. During the Fiscal Year 1990 effort would be concentrated on deriving a two dimensional transfer function between the underice environment and the ice surface viewed from above. Also important was that all funding agencies and their collaborating staff should have ready access to a quality-controlled co-located data set for further study.

## 12. REFERENCES

Comiso, J.C., P. Wadhams, W. Krabill, R. Swift, J. Crawford and W. Tucker (1989). Top/bottom multisensor remote sensing of Arctic sea ice. *J. geophys. Res.*, submitted.

Guoliang, J. and P. Wadhams (1989). Travel time changes induced in a tomography array caused by a sea ice cover. *Progress in Oceanogr.*, in press.

Wadhams, P. (1978). Characteristics of deep pressure ridges in the Arctic Ocean. *Proc. 4th Intl. Conf. on Port and Ocean Engng Under Arctic Conditions*, St. John's (ed. D.B. Muggeridge), Memorial Univ., St. John's, Nfld., 1, p544-555.

Wadhams, P. (1981). Sea-ice topography of the Arctic Ocean in the region 70°W to 25°E. *Phil. Trans. Roy. Soc., Lond.*, 302A,, p45-85.

Wadhams, P. (1988). The underside of Arctic sea ice imaged by sidescan sonar. *Nature, Lond.*, 333, p161-164.

Wadhams, P., J.C. Comiso, A.M. Cowan, J. Crawford, G. Jackson, W. Krabill, R. Kutz, C.B. Sear, R. Swift, W.B. Tucker and N Davis (1989). Concurrent remote sensing of Arctic sea ice from submarine and aircraft. *Int. J. Remote Sensing*, submitted.

Wadhams, P. and S. Martin (1989). Processes determining the bottom topography of multiyear Arctic sea ice. US Army Cold Regions Res. & Engng. Lab., Hanover, NH., Special Rept. W.F. Weeks Volume, in press.

### 13. ACKNOWLEDGEMENTS

This report was prepared by Dr C. Sear. It has been revised and expanded from the project report issued in Summer 1989 and originally prepared by Dr Wadhams. The work described and carried out by SAIC in Cambridge was undertaken by Drs Wadhams and Sear, S. Moore, A. Scoon and N. Flack.

At SAIC Cambridge, administrative support was given by Ms M. Cowan and managerial support by A. Cowan.

**APPENDIX I**

**APPENDIX II**

## CONCURRENT REMOTE SENSING OF ARCTIC SEA ICE FROM SUBMARINE AND AIRCRAFT

P. Wadhams<sup>1</sup>, J.C. Comiso<sup>2</sup>, A.M. Cowan<sup>3</sup>, J. Crawford<sup>4</sup>, G. Jackson<sup>5</sup>,  
W. Krabill<sup>6</sup>, R. Kutz<sup>2</sup>, C.B. Sear<sup>3</sup>, R. Swift<sup>7</sup>, W.B. Tucker<sup>8</sup> and N. Davis<sup>1</sup>

---

In May 1987, the first concurrent remote sensing of Arctic sea ice from the top and the underside was performed. A submarine, equipped with sidescan and upward looking sonar, collaborated with two remote sensing aircraft equipped with passive microwave, synthetic aperture radar (SAR), infrared sensor, and laser profilometer. By careful registration of the three tracks it has been possible to find relationships between ice type, ice morphology, SAR backscatter and microwave brightness temperatures. The key to the process has been the sidescan sonar's ability to identify ice type through differences in characteristic topography.

---

## INTRODUCTION

A collaborative remote sensing experiment involving a submarine and two aircraft travelling along identical tracks took place in the Arctic Ocean in May 1987. This was a unique experiment in that it was the first time that under-ice imagery as well as ice draft profiles could be compared directly with the output of ice surface remote sensing systems, including passive microwave, synthetic aperture radar (SAR), and laser profilometer. The results provide the first extensive validation of SAR and passive microwave performance in terms of definitely known ice types and ice thicknesses. The value of this

experiment lies with the varied sensor types which have been co-registered to the SAR image, such that inferences can be drawn by contrasting the signatures of the various sensors.

The submarine was equipped with an EDO Western model 602 sidescan sonar towfish, mounted on her upper casing and feeding an EDO 706 sidescan mapping system operating at 100 kHz. The submarine was also equipped with a narrow-beam 48 kHz upward-looking sonar with paper chart and digital outputs. A NASA P-3A aircraft was equipped with a set of passive microwave sensors, Airborne Oceanographic Lidar (AOL), a PRT-5 infra-red radiometer, and aerial cameras. The other aircraft was a Cessna Conquest of Intera Technologies Ltd., Calgary, Alberta, equipped with the STAR-2 X-band HH-polarization SAR giving wide swath (65 km) imagery. The Cessna flew at 10,000 m throughout; the P-3A was flown partly at high altitude (6000 m) for good spatial coverage and partly at low altitude (245 m) for good resolution and to allow use of the AOL.

The submarine undertook four 24-hour legs of ice profiling, proceeding from the North Pole towards the coast of Greenland, then eastward to the entrance of Fram Strait and southward through the Greenland Sea. Each leg was overflown close to its time of completion by the two aircraft, operating from bases in northern Canada (Alert), Greenland (Thule) and Svalbard. In this paper we report results of the analysis of a portion of the joint dataset, obtained in the heavily ridged region north of Greenland at about 85°N on May 20th. Analysis of the complete dataset will be reported in future papers.

## POSITIONING

Positioning is a critical part of the data reduction and analysis procedure, since the concurrent data were captured from three separate



platforms along a pre-arranged sampling track. The submarine, Intera aircraft and P-3A aircraft were all navigated with inertial navigation systems (INS). In addition, for the P3-A, positioning information from a Motorola Eagle Global Positioning System (GPS) receiver was recorded along with the INS data. During the May 20th mission, a four satellite GPS constellation was visible for a period of approximately 2.5 hours, during which the high altitude microwave observations were captured. Aerial photographs were also obtained with a T-11 23 cm format camera as well as with a 35 mm Flight Research camera, both of which place the time of day on an inset associated with each photograph.

Our approach to post-flight positioning was to use the GPS information and the high altitude aerial photography to register the data from the P-3A aircraft sensors to the SAR image. In the sample track length of 191 km, which is analyzed in this study, a total of 20 features (largely leads) were unambiguously recognized in both the SAR imagery and the aerial photography. We were able to reconcile points between east- and west-bound passes in the same region to within less than 300 m. During the low altitude portion of the mission, the positioning of the data was determined by using the INS information corrected with the last available GPS-determined position. We were able to correct the INS registered data through comparison of the low altitude (245 m) aerial photographs with the previously registered SAR image using 12 unambiguous features. In our estimation, the laser profiling data are registered to the SAR imagery to within  $\pm 85$  m (five SAR pixels).

The sonar records from the submarine were co-registered with the SAR imagery by matching features in the sidescan sonar image with those of the SAR. It was easy to recognize floes, ridges and leads on each set of imagery and many coincident points could be found, giving an estimated cross-track accuracy

of registration of better than five SAR pixels. The submarine track was overlaid on the SAR imagery and in this way could be compared with the P-3A track and associated data sets.

## **SENSOR COMPARISONS**

### **3.1 Active and Passive Microwave Imagery**

The microwave sensors are ideal for monitoring sea ice cover because of their ability to penetrate cloud and darkness. The passive microwave system consists of an Electrically Scanning Microwave Radiometer (ESMR) which operates at 19 GHz, and a set of multichannel sensors called Advanced Multichannel Microwave Radiometer (AMMR) consisting of 37 GHz and 18 GHz dual polarized radiometers and a 21 GHz channel operating at vertical polarization only. ESMR has a beam width of  $3^{\circ}$  and covers a spatial area from  $-45^{\circ}$  to  $55^{\circ}$  with 39 beam positions. The AMMR channels have beam widths of about  $6^{\circ}$  and were set at  $50^{\circ}$  so as to be compatible with the Scanning Multichannel Microwave Radiometer (SMMR) on board the Nimbus-7 satellite. The X-band SAR system on board the Intera aircraft has a resolution of 16 m and a swath width of 64 km. The image is presented in the form of pixels, each of which represents relative radar backscatter.

An example of coverage over sea ice by both active and passive sensors is shown in Figure 1. The P-3A aircraft was first flown from west to east at an altitude of 6,000 m. A second pass was then flown from east to west, offset so that the AMMR viewed the same area of interest at the same altitude. Finally a low altitude track at 220 m was flown over the previous AMMR track. Figure 1a shows color coded ESMR imagery collected during the high-altitude eastbound leg, Figure 1b shows the SAR image over the same general area, while

Figure 1c shows ESMR imagery collected during the westbound leg. The location of the AMMR footprint in the westbound pass is shown by the color-coded stripe in Figure 1b. Some ice features common to both sensors, especially leads and areas of first- and multi-year ice have been indicated with identifying arrows.

In the ESMR imagery, first-year ice cover has the highest brightness temperature (designated by pink) because the ice is saline, resulting in high effective emissivity. Areas of multi-year ice show much more variability with low values (light brown and orange) where the ice is relatively flat and has snow cover and slightly higher brightness temperature values (dark brown) in heavily ridged areas. Areas of open water exhibit the lowest brightness temperature (green and blue). By contrast, the SAR imagery shows low backscatter values for open water inside the ice pack, slightly higher values for thin and first-year ice, higher values for multiyear ice and the highest values for ridged ice (Lyden et al., 1984). Because they are sensitive to different physical properties of the ice, the active and passive sensors could thus complement each other and can be used to improve discrimination of different ice types. For example, whenever undeformed young or new ice is difficult to differentiate from calm open water in the SAR image because of almost identical backscatter, the passive microwave data can be used to remove the ambiguity because of the large contrast in the emissivity of these two surfaces. Also, when the snow/ice interface of a multiyear ice floe is saline, as can happen through various mechanisms (Tucker et al., 1987), the brightness temperature of this ice type would be very similar to that of first-year ice. In this case, the SAR data can be used to better establish the ice type because of the large difference in backscatter between multiyear ice and undeformed first year ice. The interpretation of first-year, multi-year ice and leads was

aided by notes taken by an ice observer during the flight and by video and still photography.

### 3.2. Comparison with sonar, infrared, and laser.

Figure 2 is a composite scene developed using co-registered upward and sidescan sonar data, X-band SAR imagery, passive microwave radiometry, and laser profiling information. The SAR (Fig. 2d) scene which is approximately 7 km by 2 km, has had a submarine ground track superimposed on it. This section was selected for presentation because it contains examples of open leads, recently refrozen leads, first-year ice, and deformed multi-year ice with well defined ridging. The upward sonar profile is shown in Figure 2b, and the analog side-scan sonar scene in Figure 2c. A profile of the SAR backscatter values extracted from the submarine track is shown in Figure 2a. Corresponding surface ice topography obtained with the AOL laser profilometer is provided in Figure 2e, along with an infra-red ice surface temperature profile from the PR7-5 (Figure 2f), and a cross-section of the 18 and 37 GHz ice emissivities acquired with the AMMR (Figure 2g). It can be seen that there are strong relationships among the signatures of the various sensors to the quite varied ice types. The center of the SAR image is dominated by a section of open lead (white arrow), a the large area of first year ice (dark green), and an expanse of highly deformed multi-year ice (yellow), especially to the west (left) of the lead, with the lightest yellow (highest backscatter) corresponding to ridges. The sidescan sonar shows mainly heavily deformed multiyear ice; we have already found (Wadhams, 1988) that undeformed multiyear ice has a unique topography of bulges or blisters which enable this ice type to be distinguished unequivocally from smooth undeformed first-year ice by the use of the sidescan.

Some inferences can be made by contrasting the signatures from the various sensors using the SAR as a convenient reference.

(1) The sonar profile (Figure 2a) beneath the lead has a "grassy" appearance on its left hand side, a result of the strong echo at the water-air interface saturating the recorder. The lead is also well defined in the sidescan sonar image as well as in the PRT-5 and AOL ice topographic profiles. The PRT-5 profile shows the elevated temperature (about  $-2^{\circ}\text{C}$ ) expected for an open lead while the AOL profile has a fine-scale characteristic of open water. The AMMR brightness temperatures of the lead at 18 GHz (vertical polarization) are low compared to those of consolidated ice. However, the brightness temperatures at 37 GHz do not show similar contrast between open water and ice because of significantly more internal scattering in the ice at 37 GHz than at 18 GHz (Comiso, 1986).

(2) The sensors show that the right side of the lead has been re-frozen. This distinction can be seen in the SAR image which has been enhanced to show contrast between the low image tone values. The contrast between the open water and refrozen lead is very difficult to determine from the SAR image because open water, young ice, and first-year ice all have low backscatter levels. Distinction between the open water and these ice types is considerably more apparent in the sonar, infra-red, and passive microwave records but is somewhat less distinct in the laser record due to the lack of relief between the targets.

(3) A positive correlation is apparent between backscatter level on the SAR image and ice thickness indicated from the sonar and lidar profiles.

(4) Interesting information can also be gathered by comparing the laser topographic profile with the sonar profile and sidescan records even though the

two profiles are offset by some 300 m. Note particularly the shape of the large pressure ridge immediately west of the open lead. The ridge is quite jagged in appearance on the laser record with a height of 3.3 m and width of 100 m, while the corresponding keel is 27 m deep, more rounded, and broader (150 m). The sidescan indicates an area of continuous ridging extending for about 600 m to the west of the lead (confirmed by the high SAR brightness values) while the upward sonar and laser both show that the first ridge in the sequence is the biggest. If we assume that this ridge does not change character between these two profiles, then we can say that the width of the keel is 1.5 times that of the sail and its height 8.2 times the height of the sail. This is within the range of variability of ridges which have been investigated by drilling (e.g. Kovaks and Mellor, 1974) and fits almost exactly a laser-sonar ridge regression found in an earlier experiment (Wadhams, 1981, eqn. 18); the small width multiplier suggests a shear ridge rather than a pressure ridge.

A distinction between the upper and lower ice surfaces can be seen by comparing probability density functions (PDFs) of the laser and sonar profile across the 7 km of track which are shown in Figure 2. The results are shown in Figure 3. It is clear that the distributions are non-gaussian. The greater breadth of the subsurface PDF over the narrower surface PDF is also apparent. The median depth of the sonar PDF is 5.38 m and the mean depth 6.34 m, while the median elevation of the laser PDF is 0.44 m and the mean 0.60 m. The ratios of means are distinctly greater than the sail to keel ratios apparent in the Figure 2 profiles, and may reflect the fact that the tracks were not identical. Figure 3b is a PDF of the SAR brightness values along the same 7 km of track as the laser (Figure 3a), while Figure 3d is the SAR PDF along the same track as

the sonar (Figure 3c).

### 3.3. Quantitative relationships

SAR pixels have an effective resolution of 5.6m (along track) x 16m (across track). The SAR pixels on original images were subsampled along track by three in order to obtain 16.8m x 16m pixels, which makes it easier for submarine and aircraft tracks to be colocated accurately and for sonar data to be compared with SAR. The original SAR brightness data, each sub-sample and the mean brightness of three sub-samples, were compared. There was no significant difference between the statistics and pdfs of these five series. It was concluded that obtaining 'square pixels' by sub-sampling would not materially affect results.

There is a clear similarity between the shapes of the SAR pdf and the corresponding laser or sonar pdfs, and we have already seen in Figure 2 how there appears to be a strong correspondence between SAR brightness and ice draft or elevation. We investigated this correspondence quantitatively as follows. The laser and sonar data were filtered so as to have the same effective resolution as the sub-sampled SAR pixels (16.8m). Preliminary work had shown that the residuals of linear regressions between SAR and laser and between SAR and sonar data, were not normally distributed and the original data required transforming (normalising) in order to validate regression analyses (Draper and Smith, 1981). In this case square root (sqrt) transformation yielded normal residuals for the SAR brightnesses and sonar drafts, while a fourth root transformation was required to yield normal residuals for the laser.

The resulting relationship (Figures 3e and 3f) is shown as a pair of

scatter diagrams. Figure 3e shows the relationship between  $\sqrt{\text{SAR}}$  brightness and  $\sqrt{\text{ice draft}}$ , while Figure 3f relates  $\sqrt{\text{SAR}}$  brightness to fourth root laser elevation [N.B. (ice draft + 1)m is used here because small zero errors in the sonar data can produce negative "drafts" under open leads, which cannot be used for a square root]. The corresponding least squares linear regression lines are also shown. In both cases, the independent variable was SAR brightness (the common data set). The results indicate that, for the single transect studied, the variances explained in transformed laser height and sonar depth by transformed SAR brightness were 15.8% and 17.1% respectively. The regression equation coefficients are not universal, since SAR calibration must be taken into account. Also, the ranges over which these relationships may hold are restricted by the fact that the upper limit of SAR backscatter values is reached at a finite ice draft, so that all greater ice drafts correspond to a saturated SAR brightness.

The results were promising enough to justify a comparison over a longer stretch of track, with the aim of determining an averaging length for SAR brightness and ice draft which will give the best and most useful correlation. Figure 4a shows a 22 km stretch of track, centered on the large lead of Figures 2 and 3, in which the SAR brightness and ice draft are shown together, each smoothed by an 84 m-wide running mean so as to display the main features of the variability more clearly. It can be seen that the peaks and troughs which correspond to identical ridge and lead systems become gradually out of synchronization as distance from the central lead increases. Possible reasons for this are:

- (i) The time shift of 3-5 hours between the aircraft and submarine permitted some ice deformation to occur;



(ii) Co-registration is inadequate at these space scales because of continuous fluctuations in aircraft and (especially) submarine speed which are recorded only in a smoothed way by the navigation systems.

We corrected this drift by a linear speed correction to the submarine, having a different slope to left and right of the central lead. The results yielded a correlation coefficient of 0.390 between "square" SAR pixel backscatter and ice draft averaged over the same 16.8 m of track.

With this larger data set we were able to window both SAR and ice draft over  $n$  pixels (i.e., an along-track distance of 16.8  $n$  meters), in order to determine the best length scale to use for SAR/draft comparisons. Figure 4b shows the change in correlation coefficient  $r$  as  $n$  increases. As we might expect,  $r$  increases with  $n$ , but there is an upper limit to the useful size of  $n$  since an excessively long track simply represents average conditions for both surfaces. It was found by inspection of scatter diagrams that the most useful value of  $n$ , in which a high correlation coefficient of 0.679 coexists with a substantial point-to-point variability, is 15. This corresponds to an averaging length of 252 m for the top and bottom surfaces. Such a distance is less than that required for the autocorrelation function of the ice bottom to go to zero (Figure 4c), and therefore represents a coherent ice regime for top-to-bottom comparison. The corresponding scatter diagram is shown in Figure 4d. Using this averaging length, the, 46% of the variance in ice draft can be explained in terms of SAR brightness variations.

Actual backscatter / depth relationships are further complicated by other factors, such as the ice roughness, salt content and snow cover. Nonetheless the relationships shown here demonstrate that a basis exists for developing statistics useful for interpreting SAR ice imagery in quantitative terms. The

potential value lies in the possibility that reasonably estimates of ice thickness distribution and variability in the Arctic may be obtained from airborne (or spaceborne) SAR surveys alone.

## DISCUSSION

A remote sensing operation in which aircraft and a submarine operate in concert has a unique value, in that it enables validation of passive and active microwave data to be carried out over large areas of ice surface, as opposed to the small number of floes which can be sampled from ice camps. The validation is possible because the submarine sonars give ice draft and ice morphology (from sidescan) information, enabling identification of ice type to be made (Wadhams, 1988). In the sample of data discussed in this paper, we can already see that a potentially useful relationship exists between SAR backscatter and ice draft and elevation. Further correlations will be discussed in future papers.

## ACKNOWLEDGMENT

The authors acknowledge the valuable support of the captain, officers and crew of the submarine and aircraft; Cdr I Williams and the staff of Flag Officer Submarines, Northwood; Dr G Burrows and Mr J Carter (Admiralty Research Establishment); Dr E Mollo-Christensen (NASA Goddard) for logistical help and advice; Dr. N Davies (Scott Polar Institute), N Flack and Miss A Scoon (SAIC - Polar Oceans Associates) for data processing; and Dr T Dod for design and installation of microwave radiometers. We are grateful for financial support to the Office of Naval Research under contract N00014-89-C-0014; the National Aeronautics and Space Administration Oceanic Processes Program; the Admiralty Research Establishment, Portland; and the Natural Environment Research Council.

## REFERENCES

- Comiso, J.C., Characteristics of Arctic winter sea ice from satellite multi-spectral microwave observations. *J. Geophys. Res.*, 91, 975-994, 1986.
- Draper, N.R. and H. Smith, *Applied Regression Analysis*, New York, Wiley, 1981.
- Kovacs, A. and M. Mellor, Sea ice morphology and ice as a geologic agent in the Southern Beaufort Sea, in *The coast and shelf of the Beaufort Sea*, ed. by J.C. Reed and J.E. Sater, Arctic Institute of North America, Arlington, VA, 113-116, 1974.
- Tucker III, W.B., A.J. Gow, W.F. Weeks, Physical properties of summer sea ice in the Fram Strait, *J. Geophys. Res.*, 92, 6787-6804, 1987.
- Wadhams, P., Sea-ice topography of the Arctic Ocean in the region 70°W to 25°E, *Phil. Trans. Roy. Soc., Lond.*, 302(1464), 45-85, 1981.
- Wadhams, P., The underside of Arctic sea ice imaged by sidescan sonar, *Nature*, 333(6169), 161-164, 1988.

## FIGURE CAPTIONS

## Cover

The front cover provides a composite scene composed of a 50 km by 37 km section of a larger X-band SAR image plotted alongside of a portion of microwave imagery acquired with the NASA ESMR from an altitude of about 6000 m. Obvious correspondence can be seen between the darker first year ice in the SAR image and the signature of the thin ice (colored pink) in the ESMR image. Other notable features that can be discerned between the two remote sensing scenes are areas of thicker and deformed multi-year ice which are seen as lighter areas in the SAR image and darker brown in the ESMR image.

Figure 1. A 40 km section of X-band SAR imagery from north of Greenland. Eastbound (line 1) and westbound (line 2) flight lines of the P-3A aircraft are overlaid on the image, as is the footprint of the AMMR (advanced multichannel microwave radiometer). False color ESMR (electrically scanning microwave radiometer) imagery from lines 1 and 2 is also shown; the flight lines mark the center of the ESMR images which extend so as to just overlap laterally. The box outlined in red shows the location of the imagery and profiles of fig. 2.

Figure 2. A 7 km section of corresponding imagery and profiles. (2a) The SAR brightness levels along the track of the submarine. (2b) The upward sonar profile of ice draft. (2c) Sidescan sonar imagery of the ice underside, with a 1000 m swath width. (2d) Contrast-stretched SAR imagery, with submarine and aircraft tracks overlaid. (2e) The AOL laser profile of ice elevation. (2f) PRT-5 infra-red radiometer profile. (2g) Microwave brightness temperatures from the AMMR.

Figure 3. (a) Probability density function (PDF) of ice elevation from the AOL profile of fig. 2e. (b) PDF of SAR brightness along a track corresponding to the P-3 flight line. (c) PDF of ice draft from the sonar profile of fig. 2b. (d) PDF of SAR brightness along track corresponding to the submarine. (e) Scatter diagram of the square root of SAR brightness versus corresponding square root of ice draft. (f) Scatter diagram of square root of SAR brightness versus fourth root of ice elevation.

Figure 4. (a) SAR brightness level and ice draft plotted together for a 22 km section of track, smoothed over 84 m. (b) Change in correlation between SAR brightness and ice draft as windowing length increases. (c) Autocorrelation function of ice bottom in region covered by fig. 4(a); dotted line is standard error. (d) Scatter diagram of ice draft against SAR brightness, windowed over 15 pixels, with regression line added. Dashed lines are 95% and 99% confidence intervals.

## AFFILIATIONS OF AUTHORS

1. Scott Polar Research Institute, University of Cambridge, Cambridge CB2 1ER, England.
2. Laboratory for Oceans, Code 671, NASA Goddard Space Flight Laboratory, Greenbelt, Maryland, 20771.
3. Science Applications International Corporation, Polar Oceans Associates division, Block A2, Westbrook Centre, Milton Road, Cambridge CB4 1YQ, England.
4. Jet Propulsion Laboratory of California Institute of Technology, 4800 Oak Park Drive, Pasadena, California 91109.
5. Admiralty Research Establishment, Southwell, Portland, Dorset, England.
6. NASA Wallops Flight Facility, Wallops Island, Virginia, 23337
7. EG and G Washington Analytical Services Center, P.O. Box 474, Pocomoke City, MD 21851.
8. US Army Cold Regions Research and Engineering Laboratory, 72 Lyme Road, Hanover, New Hampshire 03755.

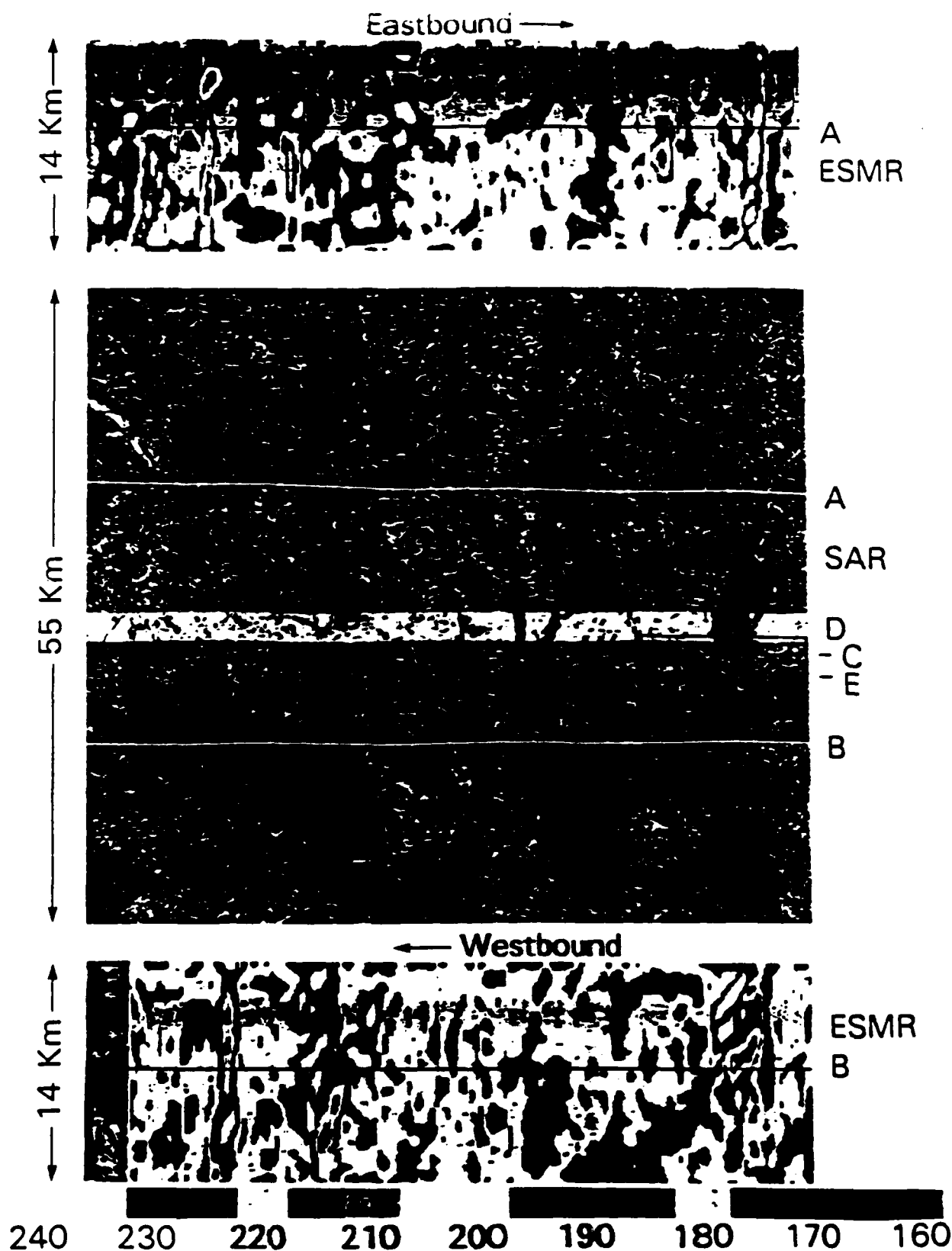


Figure 1. A 40 km section of X-band SAR imagery from north of Greenland. Eastbound (line 1) and westbound (line 2) flight lines of the P-3A aircraft are overlaid on the image, as is the footprint of the AMMR (advanced multichannel microwave radiometer). False color ESMR (electrically scanning microwave radiometer) imagery from lines 1 and 2 is also shown; the flight lines mark the center of the ESMR images which extend so as to just overlap laterally. The box outlined in and shows the location of the imagery and profile of Fig. 2.

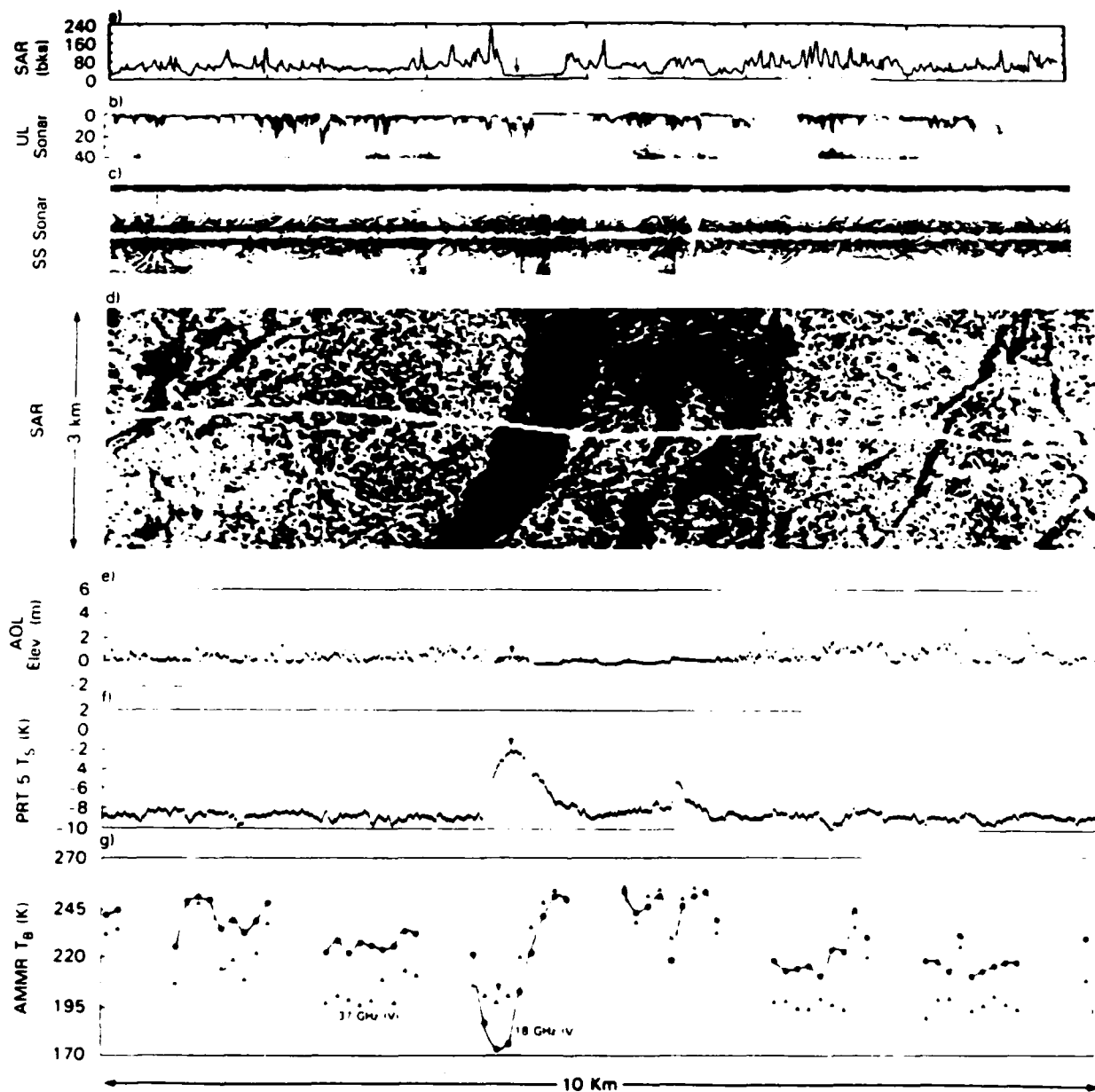


Figure 2. A 7 km section of corresponding imagery and profiles. (2a) The SAR brightness levels along the track of the submarine. (2b) The upward sonar profile of ice draft. (2c) Sidescan sonar imagery of the ice underside, with a 1000 m swath width. (2d) Contrast-stretched SAR imagery, with submarine and aircraft tracks overlaid. (2e) The AOL laser profile of ice elevation. (2f) PRT-5 infra-red radiometer profile. (2g) Microwave brightness temperatures from the AMMR.



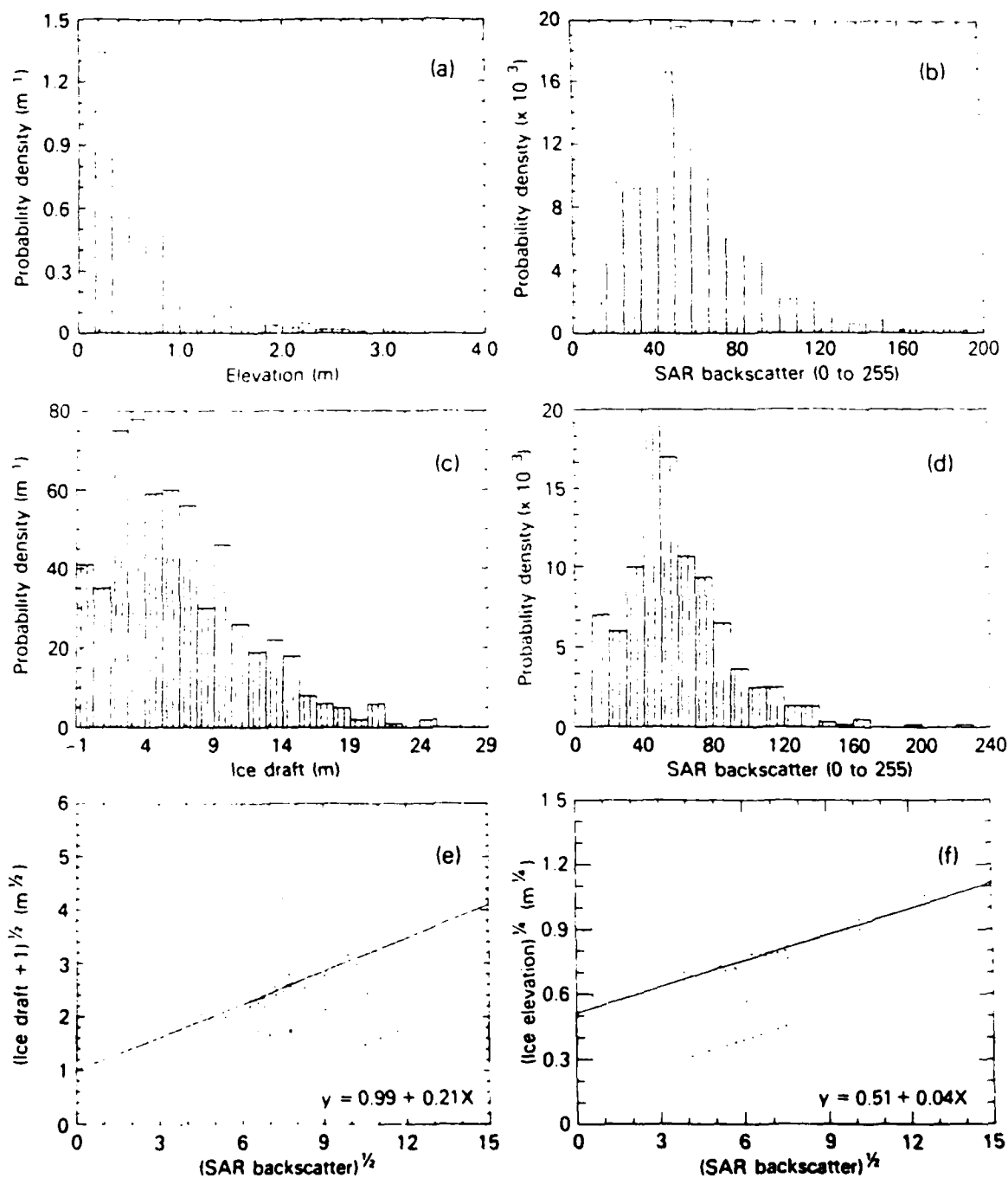


Figure 3. (a) Probability density function (PDF) of ice elevation from the AOL profile of fig. 2e. (b) PDF of SAR brightness along a track corresponding to the P-3 flight line. (c) PDF of ice draft from the sonar profile of fig. 2b. (d) PDF of SAR brightness along track corresponding to the submarine. (e) Scatter diagram of the square root of SAR brightness versus corresponding square root of ice draft. (f) Scatter diagram of square root of SAR brightness versus fourth root of ice elevation.

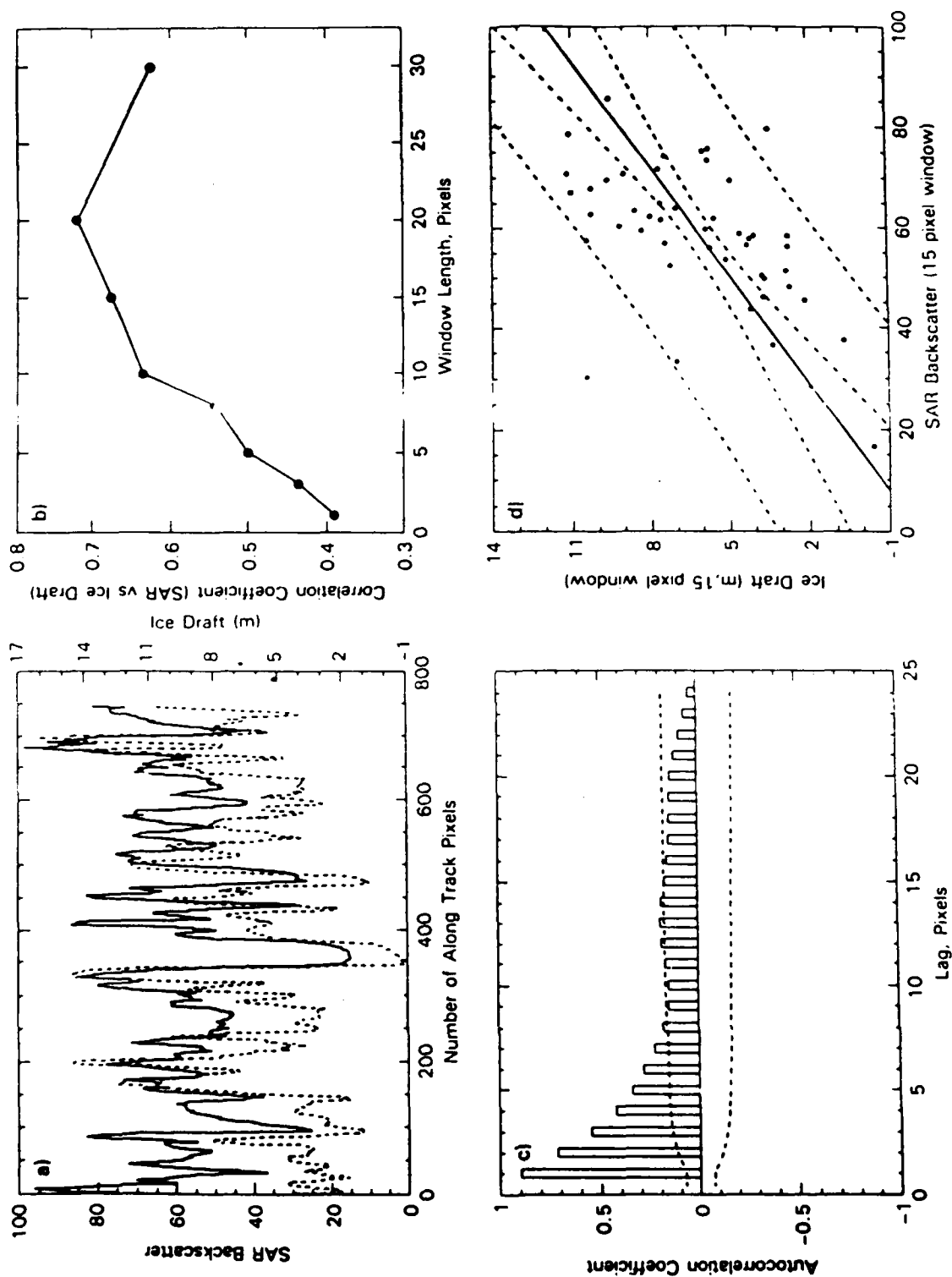


Figure 4. (a) SAR brightness level and ice draft plotted together for a 22 km section of track, smoothed over 84 m. (b) Change in correlation between SAR brightness and ice draft as windowing length increases. (c) Autocorrelation function of ice draft in region covered by fig. 4(a); dotted line is standard error. (d) Scatter diagram of ice draft against SAR brightness, windowed over 15 pixels, with regression line added. Dashed lines are 95% and 99% confidence intervals.

**APPENDIX II**

Submitted to JGR Oceans on December 22, 1987<sup>9</sup>

## TOP/BOTTOM MULTISENSOR REMOTE SENSING OF ARCTIC SEA ICE

J. C. Comiso<sup>1</sup>, P. Wadhams<sup>2</sup>, W.B. Krabill<sup>3</sup>, R.N. Swift<sup>4</sup>,  
J.P. Crawford<sup>5</sup>, and W.B. Tucker III<sup>6</sup>

### ABSTRACT

The Arctic sea ice cover has been studied using near simultaneous coverage by passive and active (SAR) microwave sensors, upward looking and sidescan sonars, a lidar profilometer, and an infrared sensor. Two aircraft and a submarine were used as platforms for this experiment. The active and passive microwave sensors are shown to complement each other as the two sensors are especially sensitive to different physical properties of the sea ice. The effects of surface roughness, derived directly from the lidar data and indirectly from the sonar data, are compared to the SAR backscatter and the passive microwave emissivity. Good correlation was found between SAR backscatter and ice draft (or elevation) especially when scales were adjusted such that 15-20 SAR pixels were averaged. Probability density functions of ice draft and elevation obtained from Lidar and sonar are also found to be superposable when allowance is made for isostasy, suggesting that the basic ice thickness distribution can be derived from the surface topography measurements alone. Undeformed sea ice, identified as first year ice, showed very little backscatter but enhanced brightness temperature due primarily to the relatively saline and therefore optically opaque surface. Comparisons of coregistered SAR and multispectral passive microwave data provided new insights into the significance of backscattered SAR signals. For example, surfaces identified as multiyear ice by the passive system have a large spread in backscatter as sensed by SAR

indicating limitations in the SAR in ice type identification. Also, ridged ice in the SAR image covers a large range of passive microwave emissivity, suggesting that ridged ice varies in age and salinity considerably. Significant variations (about 22K) in the brightness temperature of consolidated multiyear ice are observed in different regions of the Arctic with high resolution (30 m) passive microwave data. This indicates variations in texture and scattering characteristics of multiyear ice in different areas of the Arctic likely influenced by different histories of formation.

## 1. INTRODUCTION

Satellite-based microwave remote sensing systems are believed to be most suitable for studies of global sea ice cover because of their ability to operate in spite of persistent cloudiness in ice-covered regions and because of the strong contrast of the emissivity and backscatter of ice and water at selected frequencies. Multispectral passive microwave sensor data have been used for deriving geophysical parameters such as ice types and concentrations over the Arctic (Svenson et al., 1983, Cavalieri et al., 1985, Swift et al., 1985, Comiso, 1986). The potential of being able to identify different ice types in the Arctic is intriguing because an ice type is usually associated with a unique ice cover characteristic such as mean thickness. Knowledge of ice thickness is useful for several scientific applications such as calculation of mass balance and heat flux as well as some practical applications such as mineral and oil explorations and transportation. First year ice is expected to have a significantly different emissivity than multiyear ice because the former is saline and optically opaque while the latter is desalinated and optically transparent. This difference in emissivity has been the basis for the

determination of multiyear ice fraction from coarse-resolution passive microwave data assuming constant value for both multiyear ice and first-year ice. However, the apparently large variations in emissivity over the central Arctic region in winter (Comiso, 1983; Comiso, in press) suggest that the signature of multiyear ice may not be as unique as previously thought. Also, the ice concentration ( $C$ ) needs to be determined very accurately, because inside the ice pack the parameter of geophysical interest is the amount of open water ( $1-C$ ), which is expected to be only about 2% to 10% during the winter. Thus, validation of derived physical parameters from satellite data is important not only for proper interpretation of the data but also to assess the errors associated with the measurements.

Active microwave systems, especially the synthetic aperture radar (SAR), are on the other hand valuable for sea ice research primarily because they provide the ability to resolve fine details of the ice cover. Such a system was aboard Seasat which operated for only three months in 1978, but future versions of a similar system are expected; the earliest of which will be the ERS-1 SAR to be launched in 1991. Since SAR has a very high spatial resolution ( $\sim 20$  m), the data are extremely valuable in several applications including the study of ice dynamics (e.g. Hall et al., 1981). However, some ambiguities in interpretation, especially in the utilization of the digital data for ice-type classification and ice concentration retrieval, have been noted (Onstott et al., 1987). It is also not yet clear what complementary information is available from a synthesis of active and passive systems that would enable a better understanding of the characteristics of the sea ice cover.

In 1987, a unique experiment to concurrently investigate the top and

bottom features of the Arctic ice cover using sonar and microwave sensors from a submarine and two aircraft, was successfully implemented (Wadhams et al., submitted). A summary of the physical characteristics of the various sensors utilized in the experiment is given in Table 1. The British submarine was equipped with sidescan sonar having a swath width of 1 km and a resolution of 3 m, and a narrow beam upward looking sonar with an along track resolution of about 8 m. A NASA P-3A aircraft was equipped with the Electrically Scanning Microwave Radiometer (ESMR), the Airborne Multichannel Microwave Radiometer (AMMR) consisting of two dual-polarized and one single-polarized fixed beam radiometers, the Airborne Oceanographic Lidar (AOL), a PRT5 infrared radiometer, large and small format still cameras, and video recorders. Also, a Cessna aircraft of Intera Technologies Ltd., Calgary, was equipped with an X-band SAR with a swath width of 64 km and a resolution of 16 m. Simultaneous coverage of the Arctic region by the different systems was executed for a period of about 5 days. In this paper, we present an overview of the results of the experiment and a detailed analysis of a section of the ice pack where concurrent measurements were made. The submarine sensors measured thickness and bottom feature distributions which at times, provide unambiguous identification of ice type and determination of ice concentration (Wadhams, 1988). The AOL data provide roughness and freeboard information which can be correlated with the submarine data and are used for more in-depth interpretation of SAR and passive microwave data. Geophysical parameters derived from both passive microwave and SAR data are correlated with each other and compared with the other data sets which includes the PRT5 and still photography data. The importance of experiments such as this one lies in the fact that the 1990s will be a decade in which multiple microwave sensors will

be available in platforms such as ERS-1, Eos, and the Japanese and Canadian SAR satellites. If the performance of the sensors can be validated in terms of ice types and of inferred parameters such as ice thickness, then the value for synoptic monitoring of global sea ice will be greatly enhanced.

## 2. INSTRUMENTATION

The ESMR sensor on board the P-3A is a Dicke-type 19-GHz radiometer similar, but not identical to that flown on board the Nimbus-5 satellite. It has 39 beam positions, each with a beam width of  $3^{\circ}$ , and was installed so that it could scan from  $-45^{\circ}$  to  $55^{\circ}$  from nadir. This setup allowed overlap with measurements from the Airborne Multispectral Microwave Radiometer (AMMR), which was fixed at a beam angle of  $50^{\circ}$  from nadir. The AMMR consisted of two dual-polarized radiometers operating at 18 GHz and 37 GHz, and a vertically polarized 21-GHz radiometer. Calibration of these sensors was conducted with a thermally controlled blackbody and reflected sky radiance. During the high-altitude segments of the flights (6000 m), the ESMR had a resolution at nadir of about 314 m and a swath width of 14.6 km, while the AMMR radiometers had a resolution of about 1528 m by 750 m. At low altitude (245 m), the ESMR had a nadir resolution of 13 m and a swath width of 595 m, while the AMMR had a resolution of 60 m by 31 m.

The Intera STAR-2 SAR, which is an X-band system operating at HH polarization, was flown at about 10,000 m and operated in two different resolutions during the course of the experiment: one at 16 m with a swath width of 63 km, and the other at 5 m with a swath width of 17 km. In areas where repeat coverage over the same region was possible, as on May 19, 1989, wide swath data was collected followed by high resolution data passes. On May 20,



1989, the data was collected with the 16-m resolution mode only. The SAR data are digitally processed to 7 looks in near real-time on board the aircraft. The imagery is ground range corrected and represents relative backscatter in 0 to 255 gray values.

The submarine was equipped with a narrow-beam 48-kHz upward-looking sonar mounted on her fin, with digital and paper chart outputs. The output from the digitizer was used as the primary data source, with the chart output used to fill in gaps where the digitizer lost lock. The record was corrected for varying submarine speed and for depth variations by generating a sea level profile for open water cracks and leads (which gave characteristic "grassy" echoes due to high return signal strength from the water-air interface). Finally, the dataset was interpolated to 1-m horizontal intervals; this was wider than the interval between successive sonar pulses, but less than the surface beam diameter of the sonar. The latter value was about 8 m, based on the depth of the boat and nominal beamwidth of the sounder, but it is likely that the effective beam diameter was much less, since the digitizer responds to an echo which passes a certain threshold signal strength, and this tends to come from directly overhead. The submarine was also equipped with an EDO Western model 602 sidescan towfish mounted on the casing and feeding on EDO 706 mapping system generating at 100 kHz. This yielded geometrically corrected imagery of the ice underside along a 1-km-wide swath centered on the submarine track, with good-quality reflections being obtained across 600-700 m of this swath (Wadhams, 1988).

Laser profiling data were obtained with the Airborne Oceanographic Lidar (AOL) (Krabill et al., 1984) on board the NASA P-3A. A nitrogen gas laser was operated at 200 pulses per second. At the 120 m/sec aircraft velocity, this

pulse repetition rate provides observation of elevation every 0.6 m. The laser has a beam divergence of about 2.5 mrad, yielding a footprint of about 1.6 m from the flight altitude of about 200 m. Information from an aircraft inertial navigation system including attitude, heading, and velocity are recorded by the AOL along with the laser profiling data. The vertical aircraft motion must be removed from the laser profiling data prior to its use in analytical procedures. Methods have been developed which employ low-pass filtering of straight line segments connecting "low points" in the profile and subsequently subtracting these from the original profile to remove the aircraft motion (Hibler, 1972; Holyer et al., 1977). In this study, we followed the same technique, except that we manually constructed and digitized a smooth line through the minima points. These points were carefully selected to be either from very thin ice or open water areas that were identified from the aerial photographs. Although this procedure results in the removal of most of the aircraft motion, some error still remains in the profile, probably on the order of about 20 cm. However, the relative error within a few kilometers' scale is believed to be much smaller.

Physical surface temperature measurements were made with the PRT-5 sensor on board the P-3A aircraft. It has a spectral range of 8 to 14 microns, a 2-degree field of view, and a design accuracy of  $0.05^{\circ}\text{C}$ . The sensor was calibrated inside a controlled chamber before and after the mission. However, this particular unit had a noise level of about 3 K making it difficult to detect fine variations in temperature over the ice surface. Nevertheless, it was sensitive enough to detect fluctuations caused by the occurrences of leads and new ice within the ice pack.

The errors in measurement are different for the different sensors. The

measurement error for the ice elevation from the lidar data is estimated to be about 20 cm, including errors in the retracking. For the passive microwave radiometers, the calibration was done using the sky as a cold reference and a blackbody as a hot reference. However, the absolute calibration might change after take-off and the amount of change introduced in the process is not precisely known. The relative precision, however, is estimated to be on the order of 2 K. As for the SAR, the absolute calibration is not known making it difficult to use a radiative transfer model to interpret the results. The errors associated with the upward-looking sonar stem from imperfect removal of submarine depth variations and from the effect of sonar beamwidth in broadening the apparent dimensions of pressure ridges. Beamwidth effects are discussed in Wadhams (1981) but are likely to be minimal in the present case because of the narrow beam; we estimate an error of  $\pm 20$  cm due to imperfect depth correction. From the laboratory study of the sensitivity of the PRT5, the physical temperatures observed can be off by as much as 3 K. However, the relative precision is probably better, judging from its response to the various surfaces.

### 3. FLIGHT TRACKS AND REGISTRATION OF DATA

The flight tracks of the two aircraft were designed to maximize our ability to do correlation studies of top surface information derived from aircraft data with bottom surface characteristics derived from submarine sonar data. The different platforms were all equipped with inertial navigation systems which has an accuracy of about 1.5 km. For detailed comparison of data from different platforms, much better accuracy is required. Fortunately, the imaging systems from the various platforms provide enough information to allow

spatial registration of the different images. The NASA P-3A aircraft was also equipped with Motorola Eagle Global Positioning System (GPS) which provided surface location accuracies of about 30 to 50 m.

The flight tracks of the NASA P-3A aircraft during three successive days are shown in Figure 1. The flights were generally flown at an altitude of 6000 m, but segments of these flights were conducted at 200-245 m to enable AOL ranging measurements. On May 19, 1987, the aircraft took off from Thule, Greenland, flew all the way to the North Pole, and back to Thule along approximately the same track, collecting almost 6 hours of continuous measurements. On May 20, 1987, the aircraft took off at Thule, went around the Lincoln Sea region for measurements at both high altitude and low altitude, and then flew through Fram Strait, landing at Longyearbyen, Svalbard. The following day, the aircraft took off from Longyearbyen, flew to about  $87^{\circ}\text{N}$ , and then around approximately the same track as the previous day. Other flights included several passes through the Fram Strait and over the Greenland Sea region. This paper will focus primarily on results from the May 20 data. The flight mission during this day included a section of overlapping passes beginning near  $40^{\circ}\text{W}$  and extending to  $10^{\circ}\text{W}$  (see Figure 1). The initial pass was made from west to east at a flight altitude of about 6000 m. A pass at the same altitude was then made from east to west followed by a low altitude pass flown from west to east at an altitude of about 200 m.

To spatially register the NASA P-3A data with the Intera SAR, the GPS positioned 35-mm and 229-mm format photographs were utilized. Prominent features, such as leads, pressure ridges, and ice-rafted structures between large ice masses seen in the 35-mm and 229-mm photographs were co-registered with the same features in the SAR images. About 25 such features over a 100-km

track were identified on both the SAR image and aerial photography allowing the GPS referenced points on the aerial photos to be precisely located on the SAR image. To assess the location accuracy, the relative positions on the SAR images were compared with the GPS-determined positions of the respective points. In this process, the endpoints were assumed to be correct and the remaining points were compared in a relative sense. The results are shown in Figure 2, where the measured position of the features from the SAR imagery are plotted along with the positions determined from the GPS. The P-3A low-altitude (245 m) track was registered in a similar fashion. However, the task was slightly more difficult because the photography covered a much smaller area and the features were not as easily recognized.

Errors in registration cannot be avoided, especially for our case where we have to deal with measurements from different platforms, each with different footprint sizes and taken at different speeds. What is comforting is the fact that the analysis (see Figure 2) indicates an error of, at most,  $\pm 15$  SAR pixels. Furthermore, in some of the comparative analysis involving a few kilometer tracks, a slight registration error was found not to be critical to the proper interpretation of the results. Because of scaling (as will be discussed later), the statistical results and conclusions were basically the same, even when the SAR pixels were shifted in one direction by one or two pixels.

#### 4. COMPARATIVE ANALYSIS OF DATA FROM THE VARIOUS SENSORS

A typical example of near-simultaneous active and passive microwave data collected during the mission is shown in Plate I. The top and bottom images are from the ESMR sensor collected during the high-altitude passes of the P-3A

aircraft north of Greenland, while the middle image is the corresponding SAR coverage over the same general region. The aircraft was flown from west to east following the track labeled A and then from east to west along track B with the AMMR footprints in both passes covering approximately the same area, which is shown in the SAR image as a yellow stripe (for the west to east pass). A third pass over the same general area was flown from west to east at low altitude (220 m) over the track labeled C (red line) for which laser profile data was collected. The same general characteristics of the ice cover are evident from both active and passive sensors. In the SAR image, low backscatter values (black) are seen in areas of open water, refrozen leads and first-year ice, while a relatively higher backscatter (bright) is observed over undeformed multiyear ice and ridged ice. In the color-coded ESMR images, open water exhibits low brightness temperatures (blues and greens), first-year ice has the highest brightness temperatures (pink and red), while multiyear ice and ridged ice have intermediate values. The difference in the detection of the surface is caused primarily by the sensitivity of the two sensors to different physical properties of the ice cover. In this sense, the two systems can be used in conjunction to improve discrimination of different ice surfaces. For example, whenever undeformed ice or new ice is difficult to differentiate from calm, open water in the SAR image because of almost identical backscatter, the passive microwave data can be used to remove ambiguity because of the large contrast shown in the emissivity of these two surfaces. Alternately, when the snow/ice interface of multiyear ice is saline, as can happen through various mechanisms (Tucker et al., 1987), the brightness temperature of this ice type would be similar to that of first-year ice. In this case, the SAR data could resolve the ambiguity because it clearly shows the difference in surface

roughness (or backscatter) of these two ice types.

To improve our understanding of the SAR backscatter and the passive microwave radiances, a section of the data is studied in more detail using multisensor measurements. A composite scene using data from various sensors over a 10-km region of that shown in Plate 1 (see red box) is presented in Plate 2. The tracks of the P-3A and the submarine were not exactly coincident for the segment shown in Plate 2. However, the tracks were close enough (in this case about 300 m apart) to enable meaningful comparisons to be made, especially with the aid of the imaging systems (SAR, ESMR and sidescan sonar). This section was selected because it contains examples of open leads, recently refrozen leads, first-year ice, and deformed multiyear ice with well-defined ridging. In general, the data shows much higher concentrations of multiyear ice. A profile of the SAR backscatter values extracted from the submarine track is shown in Plate 2a. The upward-looking sonar profile is shown in Plate 2b, and the analog side-looking scanning sonar is in Plate 2c. The SAR image which is approximately 10 km by 3 km, is shown in Plate 2d with the submarine track superimposed on it. Corresponding surface topography obtained with the AOL profilometer is provided in Plate 2e, along with a temperature profile derived from the PRT-5 infrared sensor (Plate 2f). Finally, a cross-section of the 18 and 37 GHz brightness temperatures acquired with the AMMR is presented in Plate 2g.

The SAR image (Plate 2d) shows highly variable signatures for the ice in this region. The center is dominated by a section of open lead (white arrow), a large area of first year ice (dark green), and an expanse of highly deformed multiyear ice (yellow), especially to the west (left) of the lead, with the lightest yellow (highest backscatter) corresponding to ridges. The plot shows

the expected large variability and relatively high SAR backscatter values over ridged and undeformed multiyear ice. However, because of the backscatter over open water, the newly refrozen lead, and first year ice, are all low and lacking contrast, the distinction of these ice types is not so apparent.

The upward looking sonar profile shows a characteristic "grassy" appearance at the lead location, a result of the strong echo at the water-air interface saturating the recorder. The lead is also well defined in the sidescan sonar image as well as in the PRT-5 and AOL profiles. Undeformed multiyear ice has a unique topography of bulges or blisters (Wadhams, 1988) which enable this ice type to be distinguished unequivocally from smooth undeformed first year ice. An enlarged version of a section of the sidescan image together with the corresponding SAR image is shown in Figure 3. Arrows are provided to indicate identical features in the images.

Large contrast in the brightness temperatures of the lead and consolidated ice as measured by the AMMR at 18 GHz is evident in Plate 2g. A similar effect is not apparent at 37 GHz, especially between the lead and multiyear ice because the radiation (at 0.8-cm wavelength) is more vulnerable to internal scattering. In the lead area, the 18 GHz brightness temperature value is lower than that of the 37-GHz, but over the multiyear ice region, the reverse is true. In the first-year ice region, the values are almost the same. The gaps in the AMMR data correspond to the time period when data could not be collected because the data acquisition system is busy digesting current data and transferring them to a mass storage unit. A more quantitative comparison of the observations of the same study region by the different sensors is presented in the following sections with the last section devoted to "scaling," a topic which we feel is important in order to truly understand the meaning of a measurement especially in relation with other measurements.



#### 4.1 Bottom Topography versus Laser Profile

It was found by careful co-registration of the P-3A flight track and the submarine track using the SAR imagery as a matrix, that the tracks of the aircraft and the submarine were separated laterally by an average of about 300 m, although a maximum separation of about 1 km was observed in some locations. The temporal separation ranged from zero to 24 hours. The near coincidence in the collection of data made it seem worthwhile to attempt a joint statistical analysis of the laser and sonar datasets using quite short (20 km) sections of track, as opposed to the longer (100 km) sections that were used for a similar analysis following a 1976 submarine/laser experiment where the airborne navigation was not as accurate (Wadhams, 1981). We report here on the results of analyzing three consecutive 20 km sections from north of Greenland at about  $85^{\circ}\text{N}$ . This is within the same region, described earlier and investigated intensively in Wadhams et al. (submitted, 1989), where co-registration was especially good.

The sections will be designated 1, 2, and 3. First, we examine ice draft and elevation distributions. All three sections were taken from a heavily ridged zone of mainly multiyear ice which occurs north of Greenland due to the long-term average motion of the Trans-Polar Drift Stream and Beaufort Gyre driving ice against the land boundary (Hibler, 1979). Such a zone of heavy ridging has been found in earlier datasets (Wadhams, 1980, 1981, and 1983a). Drafts were classified in 0.1-m increments. As Table 2 shows, the mean ice draft did not vary greatly among the three sections, although for section 3 it was slightly deeper. The modal drafts had an opposite trend, varying from 2.9 m for section 1 to 2.1 m for section 3. The mean elevations of the

corresponding laser sections have an opposite trend from those of the sonar sections, while the modal elevations vary in similar fashion to those of the sonar. The earlier sonar/laser experiment (Wadhams, 1981, Figure 10) showed a clear, positive correlation between mean draft and elevation of corresponding 100-km sections, but with considerable scatter. We expect a similarly positive correlation when we come to compare all 2000 km of concurrent sonar and laser data, but for such a small number of sections the scatter is dominant, and is presumably due mainly to the variable amounts of snow cover (which influence elevations much more than drafts) as well as to the detailed mismatch between aircraft and submarine tracks.

If the overall mean drafts of sections 1, 2, and 3 are compared with the overall mean elevations, the ratio is 7.91. This ratio  $R$  should be related to mean ice and surface water densities  $\rho_i$  and  $\rho_w$  by

$$R = \frac{\rho_i}{\rho_w - \rho_i} \quad (1)$$

If we assume a surface water density of  $1025 \text{ kg m}^{-3}$  (typical of Arctic surface waters but possibly an overestimate if melt has begun), then this gives a mean ice density of  $910 \text{ kg m}^{-3}$ , close to the value found by Wadhams (1981) of  $915 \text{ kg m}^{-3}$  by a similar draft/elevation comparison.

When the distributions of ice draft and elevation are plotted (Figure 4), a number of interesting effects are seen. The three distributions of drafts are very similar in shape; divergence occurs only at deep drafts, with section 3 having more ice than sections 2 and 1 (although there are one or two very deep keels in section 1 which cause its distribution to recover at the greatest

depths). The fall-off in probability density with draft is approximately a negative exponential at deeper drafts, in agreement with earlier observations (e.g., Wadhams, 1983b). The three distributions of elevation are also very similar in shape throughout the elevation range, with the fall-off with increasing elevation being very clearly a negative exponential at all elevations exceeding 1 m. Again, this agrees with earlier data (Wadhams, 1976, 1980, 1981) and is due to the fact that pressure ridges themselves follow a negative exponential distribution of height and tend to be geometrically congruent in shape.

The apparent congruence between the draft and elevation distributions was tested further by plotting the mean of the three draft distributions and the mean of the three elevation distributions together, with the horizontal scale of the elevation distribution expanded by a factor of 7.91. The result of this coordinate transformation (Figure 5) is in such close agreement that we can conclude that the ice cover behaves as if surface features were magnified by a factor of  $R$  on the underside, with no radical redistribution of the ice away from point-for-point isostasy. This does not mean, of course, that every point on the ice surface has a draft of 7.91 times its elevation. What it does mean is that if a fraction  $F(h)$  of the ice cover has an elevation in the range  $h$  to  $(h + dh)$ , then the same fraction  $F(h)$  will have a draft in the range of  $7.91 h$  to  $7.91 (h+dh)$ . This enables us to conclude with some confidence that in ice covers typical of the central Arctic, it is possible to derive the probability density function of ice draft (and thus of ice thickness) solely from the results of airborne laser profiling. This result has important implications: since airborne surveys are easier to conduct than submarine surveys, it greatly enhances our ability to synoptically monitor the ice thickness distribution in

the Arctic in order to test for evidence of thinning in response to greenhouse warming.

Independent ridges were identified using the Rayleigh criterion (e.g., Wadhams, 1983a) in which an independent keel is one in which the troughs (points of minimum draft) on either side of the keel crest each rise at least halfway towards the local level ice bottom before beginning to descend again. For keels, the real-level ice bottom is defined arbitrarily (but consistently with previously published work) as being a draft of 2.5 m. Sails are defined similarly, except that the sail height was calculated above the laser profile zero datum, which presumably is sea level. The justification for using sea level is that the ice surface is frequently flooded alongside ridges. Figure 6 shows the distributions of keel drafts and ridge elevations, and the relevant statistical parameters are given in Table 2. It can be seen that the distributions all follow approximately a negative exponential form, as found in many previous studies, and that there is some correlation between sail and keel distributions for corresponding sections. This is masked, however, by the small numbers of keels and sails involved in a 20-km section, and by the fact that the three sections are very similar in their properties.

Once again, to investigate more closely we combined sections 1, 2, and 3 and directly compared the resulting keel depth and sail height distributions. Results are shown in Figure 7. The two distributions have become better approximations to negative exponentials: i.e., to

$$n(h) dh = A \exp(-ah) dh \quad (2)$$

where  $n(h)$  is the number density of ridges per unit distance and unit height

increment, and  $A$ ,  $a$  are parameter characteristic of the ice regime. It is clear that stretching the laser distribution by a factor of 7.91 does not superimpose it on the sonar distribution. This is to be expected since we are dealing with numbers of distinct features. With a negative exponential it is not even possible to define a single mean elevation or frequency, since these depend on the value taken for a cutoff  $h_0$  which separates genuine ridges from random fluctuations in roughness. Table 2 shows that mean frequencies and elevations/drafts depend strongly on  $h_0$  and cannot be directly compared.

Figure 6 does, however, suggest an empirical technique for converting from sail to keel distributions, although confirmation of its general validity will require longer datasets in more varied ice conditions. Using suffices  $t$  and  $b$  for top and bottom surfaces in equation (2), we find that the ratios of slopes of the two negative exponentials in Figure 7 gives us  $a_t/a_b = 6.3$ . By stretching the abscissa of Figure 7 by this factor we find that the ratio  $A_b/A_t = 9.0$  causes the distributions to be superimposed. The use of these ratios will therefore convert a sail distribution of form (2) into a corresponding keel distribution.

#### 4.2 Comparisons with Active Microwave Backscatter

Since active microwave data first became available for sea ice studies, it has been suspected that they would delineate ridge features quite clearly. As Plate 2 indicates, there appears to be reasonable correlation between the laser elevation profile and the SAR backscatter. The objective of this analysis was to assess the degree to which we can derive quantitative information about the topography of the upper and lower ice surfaces from the SAR backscatter. We begin by considering the upper surface as delineated by the AOL.

Approximately 125 km of AOL elevation data which have been registered to the SAR image, including the sections presented previously, were analyzed. Because we are interested in determining whether relationships exist that are universal in nature, we carried out the analysis on this entire length of track rather than on specific sections of interest. The AOL versus sonar comparisons described in Section 4.1 were conducted on a subset of this 125-km track.

Initial investigations were directed at cross-correlating the mean elevation and standard deviation of elevation directly with the SAR backscatter. This required calculating the mean and standard deviation of elevation for a 16.8-m window, corresponding to the SAR along-track pixel dimension. The number of elevation data points in this interval varied from 32 to 34 depending upon aircraft groundspeed. The results were not encouraging. Correlation coefficients for both the mean elevation and standard deviation were less than 0.15. Further examination of the plots of elevation, standard deviation and backscatter as a function of distance convinced us that there was little correlation at this high resolution over the track as a whole. Certain areas of the track did appear to exhibit reasonable correlation, however. These were primarily areas containing new and refreezing leads such as those shown in Plate 2. The response of the SAR signal to ice characteristics other than roughness measured by the AOL and errors in registration may have contributed to the lack of correlation.

Larger along track averaging windows significantly improved the correlations. Also, because of uncertainties in cross-track registration, for each along-track point point, a mean SAR backscatter for 5 cross track pixels was generated for the along track comparisons. Figure 8 shows cross correlation coefficients of the mean elevation versus the mean backscatter, the

standard deviation of elevation versus the mean backscatter and the elevation standard deviation versus the backscatter standard deviation for several averaging window lengths. It is evident that window lengths of 1.0 and 2.0 km provide the best correlation coefficients. Also apparent is that mean elevation versus the mean backscatter and that both of these are considerably exceeded over the correlations obtained between the standard deviations of elevation and backscatter. The effect of averaging the elevations over window lengths of 1 to 2 km is to transform the original distribution from a log normal into a normal distribution while that of averaging the backscatter provides only a slight skewing of the original normal distribution.

The mean elevation and mean backscatter for the 1 km averaging window are shown for the entire track in Figure 9. It is obvious that there are both areas of high and low correlation along the track. In particular, the correlation seems to be best for areas of low elevation. These are regions which contain significant portions of open water, young ice, and first year ice as those shown in Plate 2. Regressing the mean elevation to the mean backscatter (Figure 10) for the 1 km averaging window resulted in a best fit regression line with a correlation coefficient of 0.51. Likewise, regressing standard deviation of elevation to the mean backscatter provided a best fit coefficient of 0.48.

Needless to say, the relatively low correlation coefficients between the backscatter and topography were disappointing in that only 26% of the variance in the backscatter can be explained by the elevation and even less by the standard deviation of elevation. It must be remembered, however, that the SAR is responding to features other than elevation of the surface whereas the AOL is reflecting directly from the surface, be it ice, snow or open water. SAR is

capable of penetrating the snow surface, and the backscatter is dependent, among other characteristics, on brine and air volumes of the near surface ice as well as the small scale (<10cm) surface roughness. While the backscatter is expected to be fairly large from some ridges because of enhanced scattering cross sections in the backwards direction, it is not well understood why other ridges have significantly lower backscatter. However, recent results by Holt et al. (1990) show that lower frequency SAR (0.440 GHz) is superior in the delineation of ridges than the higher frequency versions (e.g., 5.35 GHz). It could be that the typical roughness characteristic of ridges are more suited for wavelengths longer than the X-band wavelength. Furthermore, the orientation of the ridges and size of the blocks have been observed to be important factors affecting the backscatter. Ridges aligned parallel to the flight track appeared to be more prominent than those aligned orthogonal to it.

We now consider the relationship between SAR and the upward sonar profile. We might expect a better correlation here because (a) the draft difference between first-year and multiyear ice is much greater than the freeboard difference, and (b) the sonar sees the mean structure of a ridge as opposed to its sail alone, while the SAR, because of its penetrating power in dry snow and desalinated ice, also sees a wider part of the ridge rather than merely its sail.

The analysis of SAR versus sonar was developed in the first paper on the expedition results (Wadhams et al. submitted) and is summarized here. The basis of the comparison was a 22-km coregistered track section using SAR pixels subsampled by three in order to obtain a 16.8 m by 16 m pixel size; and sonar drafts averaged over the same gauge length. Figure 11a shows the SAR brightness and ice draft displayed together, with further smoothing by an 84-m



wide running mean to show the main features of the variability more clearly. It can be seen that there is a clear, strong correspondence between the two records, but that the peaks and troughs which correspond to identical ridge and lead systems become gradually out of synchronization as distance from the central major lead increases. This due to either the 3 to 5 hour time shift between the two recordings, which would have permitted some ice deformation to occur, or to remaining errors in co-registration over short length scales caused by rapid fluctuations in aircraft and submarine speeds which are smoothed out by the navigation systems. We corrected this drift by applying a linear speed adjustment to the submarine data, and obtained a correlation coefficient of 0.390 between SAR backscatter level and ice draft using the 16.8-m pixel as the gauge length.

Next we examined the effect of windowing the data with a number  $n$  of pixels, to determine the scale length which gives the best SAR/sonar correlation. Figure 11b shows the effect of increasing  $n$  on the correlation coefficient  $r$ . As we might expect,  $r$  increases with  $n$ , but there is an upper limit to the useful size of  $n$  since an excessively long track simply represents average conditions for both surfaces. It was found by inspection of scatter diagrams that the most useful value of  $n$ , in which a high correlation coefficient of 0.679 coexists with a substantial point-to-point variability, is 15. This corresponds to an averaging length of 252 m for the top and bottom surfaces. Such a distance is less than that required for the autocorrelation function of the ice bottom to go to zero (Figure 11c), and therefore represents a coherent ice regime for top-to-bottom comparison. The corresponding scatter diagram is shown in Figure 11d. Using this averaging length, 46% of the variance in ice draft can be explained in terms of SAR brightness variations.

We note that the averaging length of 252 m is much less than the 1-km track necessary to give the best results in AOL/SAR comparisons, and that the corresponding correlation is higher (0.679 compared with 0.51). As predicted above, this is probably because ice draft offers a more direct correlation with SAR than elevation through the greater range of depth discrimination for undeformed ice and the better representation of ridges. Therefore, a high correlation can be developed over a relatively short averaging length, whereas the laser data require an averaging length which includes some major features such as large ridges or leads to give sufficient variability.

#### **4.3 Comparisons with Passive Microwave Brightness Temperatures**

The low altitude AMMR data provides a unique opportunity to examine the brightness temperature of various sea ice surfaces without having to uncouple the contributions from different surfaces (or ice types) with a mixing formulation. A footprint of about 30 m at this altitude enables direct evaluation of the observed values corresponding to signatures of pure ice types and surfaces, and direct comparison with measurements from SAR and the other sensors. A scatter plot of 18 GHz versus 37 GHz at vertical polarization for a 45-km stretch of data including those shown in Plate 2 is presented in Figure 12a. Practically all the data points lie along a line between two points labeled MY and FY. These data points correspond to consolidated sea ice covers of any type or mixtures of types as can be confirmed by visual inspection of SAR, photography, and sonar data. From the slope of the cluster of data points, it is also apparent that variations in emissivity of consolidated ice are larger at 37 GHz than at 18 GHz, the difference being due to higher sensitivity to internal scattering within the ice at 37 GHz than at 18 GHz, as

mentioned earlier. The data points between MY and FY could come from mixtures of pure signals from a MY and FY types of surfaces. However, they may result from pure signals from other types of ice surfaces as well. To evaluate the statistics associated with these different possibilities, the same data points are plotted for SAR versus the 37-GHz channel and are presented in Figure 9b. The much larger scatter of data points in Figure 12b than 12a indicate that the SAR backscatter values are not well correlated with the microwave brightness temperatures. Even the data points which have the lowest brightness temperatures at both the 37 GHz and the 18 GHz channels and normally interpreted as signatures for approximately pure multiyear ice types have very large variations in the SAR values. It is clear that some of the data identified in the SAR as ridged ice are observed by the passive microwave sensor as having the same signature as the undeformed multiyear ice. This is likely due to low salinity for these types of ridged ice suggesting that they have survived more than one summer. Except for a few speckles in the SAR images, the high backscatter values usually correspond to areas of ridging. Since high SAR values are found in the graph in Figure 12b practically anywhere between MY and FY along the abscissa, the ridged ice signature may be different in different multiyear ice areas.

To better understand what the data points between MY and FY in the scatter plot really mean, ice classification was performed within each AMMR footprint using the sidescan sonar images. The types of surfaces which could be identified by visual inspection are new ice, first-year ice, multiyear ice, ridged multiyear ice, and ridged first year ice. The result of this analysis is shown in Figure 13. The ice types are plotted versus the brightness temperature at 37-GHz vertical polarization. Although brightness

temperatures are plotted, the spatial variation in physical temperature of the same types of ice are expected to be negligible within this distance (of a few kilometers). Thus, observed variations in brightness temperatures are expected to be variations in emissivity. The results are quite intriguing, especially because the interpretation of some of the sonar data points (solid points) are considered unambiguous. The multiyear ice is shown to have brightness temperatures ranging from 187 K to 250 K, with most of the data points between 190 K and 220 K. This indicates that the variability of brightness temperatures in the AMMR plots is not due solely to variations in the mixing of different ice types and surfaces. The implication is that the signature of multiyear ice is really not unique as suggested by previous analysis of satellite data (Comiso, 1983; Comiso, 1986; Comiso, in press). The distribution for ridged ice also shows large variations, suggesting that some of this type of surface may have survived at least one summer. Although the ice that was ridged was likely first-year or young ice, the actual age of the ridge may be longer than one year. There are also several data points midway between MY and FY. This means that there is considerable variation in physical and structural characteristics of ridged ice, even within distances of a few km.

Significant variations in the emissivity of multiyear ice are already apparent within the few-kilometer track studied, as indicated in the spread of the data points shown in Figure 13. To further study the spatial variability of emissivity, high-resolution AMMR data from areas in the Arctic which are more widely separated were examined. Scatter plots of 18 GHz versus 37 GHz are plotted in Figures 14a, 14b, and 14c for the periods May 19, May 20, and May 21, respectively. The locations of the low-altitude segments of the flights

where the high-resolution data were obtained for the indicated dates are shown in Figure 1. The brightness temperatures have been converted to emissivities using PRT-5 physical temperature data to better quantify radiative characteristics of the emitting ice surfaces. The results show considerable change in emissivity from one area of the Arctic to another. At about 50 m resolution, it is expected that the footprints are small enough to resolve at least some large multiyear ice floes. It is apparent from the three plots that there is a significant shift in emissivity from one region to another. The change in emissivities correspond to areas where similar gradients in brightness temperatures are observed in the satellite passive microwave data (Parkinson et al., 1987; Comiso, 1986). These results thus further reinforce the notion of different multiyear ice signatures in different areas of the Arctic.

The data set also provides the opportunity to compare passive microwave signatures of the ice at different resolutions. Most of the passive microwave data were collected at high elevations in which the footprint sizes are about 1 km. A set of scatter plots similar to those shown in Figure 12 are presented in Figure 15a through 15d for both vertical and horizontal polarizations. The plots indicate features very similar to those of the high-resolution data but indicate a slight shift in the values. The use of larger footprints causes the lowest emissivity values to be slightly higher and the highest emissivity values to be lower, as expected. The scatter plot for SAR versus the 37-GHz channels show less scatter in the data points and better correlations for consolidated ice (first-year or multiyear ice). However, the effect of ridging is still obvious from the data and is shown as higher values for SAR. Although these high values are not pure signals from ridges because the horizontal size

of these features are normally much less than a kilometer, they indicate the strong effect of ridging on SAR backscatter in ice covered regions. A larger correlation of consolidated ice data between SAR and passive microwave measurements at this larger footprint is also apparent. This indicates, as with the case of the elevation and draft data, that there is a preferred scale at which correlation studies become more meaningful. At this footprint, some of the high-frequency variations in the microwave characteristics of the ice have been averaged in and therefore only general features are compared. It is these more general radiative characteristics which makes the SAR and passive microwave systems complementary to each other.

#### 4.4. Scaling

The results presented in the previous sections show that different correlation coefficients were obtained in the comparative analysis when different scales were used. There is a fundamental reason for this. The ice cover is actually a conglomerate of different surface types including first-year ice, multiyear ice, ridges, new ice, and open water. The sizes and dimensions of these different surfaces are different. Thus, statistical sampling could be biased when the distance studied is comparable to the size of the surface. For example, some features of multiyear ice are not so apparent with some sensors for scales as small as a few meters. However, when the scale is extended to cover large enough lengths so as to reveal the unique topography of multiyear ice, the correlation would improve simply because the unique characteristic of the particular ice type is more completely represented. Large scales, however, have some pitfalls. Some features of the ice cover, such as ridges and leads, are quite narrow. By taking scales of the order of a

few kilometers, in areas where the ridges and leads are only a few meters wide, the small features from these surfaces are overwhelmed by the larger features and may not get adequate representation in the analysis. Nevertheless, more often than not, this predicament cannot be avoided, especially for scales like those associated with satellite footprints from passive microwave sensors and AVHRR. Even considering just the change in scales from the low-altitude to high-altitude measurements with the passive sensors, it is already evident that the range in values are different. If the difference is due to the averaging over the same type of ice cover, the problem would be minimal. However, the fact that small-scale features like leads are in the averages makes it difficult to identify the real signature of a pure ice type in the large scale measurements, knowing that the signature is not really unique. It is thus necessary to understand how such small scales affect averages over larger scales before an average can be used to represent the signature of a certain surface.

## 5. DISCUSSION AND CONCLUSIONS:

The correlations described in this paper fall into two classes: (i) quantitative correlations between profiles: i.e., ice draft (sonar), ice elevation (laser), and SAR backscatter along the track line, and (ii) qualitative and semi-quantitative correlations between corresponding areas of imagery: i.e., passive microwave, SAR, and sidescan sonar.

In the profile comparisons, we have obtained the following main results:

1. Draft versus elevation comparisons yield probability density functions of similar shape which can be directly superposed when the elevation distribution is stretched and flattened by an appropriate isostatic correction factor

derived from the experimentally measured mean draft and elevation. If confirmed by data from other ice regions, this offers the possibility of using a laser alone as a means of generating approximate ice thickness distributions for the Arctic. The distributions of sail height, keel depth, and of ice draft/elevation at great thicknesses all follow a negative exponential form, with some correlation between sails at keels.

2. Draft/elevation versus SAR backscatter comparisons yield a clear, positive correlation on a statistical basis, although careful examination of correlated tracks shows that there are some ridges, for instance, for which the SAR backscatter is low. For ice elevation (AOL data) the correlation coefficient between laser-derived elevation and SAR backscatter is only 0.15 using single 16.8-m pixels as gauge length, but rises to 0.51 using a 1-km along-track averaging window and the average of 5 cross-track SAR pixels. For ice draft (sonar data), the correlation is better, being 0.39 for a 16.8-m gauge length rising to 0.68 for a 252-m along-track averaging window.

The fact that ice draft has a better correlation with SAR backscatter than ice elevation does, despite the fact that both the SAR and AOL are directed at the upper surface is at first puzzling. However, the AOL reflects directly from the snow surface, whereas SAR penetrates the snow surface and gives a backscatter which is dependent on brine and air volumes of the near-surface ice, small and large-scale ice roughness, and the orientation of the ridges with respect to the SAR antenna. There is evidence that the SAR responds to a greater width within a pressure ridge than is given by the sail alone; i.e., something closer to the width of the keel. This response to the whole of a ridge, plus the greater discrimination in draft than freeboard between undeformed first-year and multiyear ice, both act to ensure that ice draft



offers a better correlation with SAR than freeboard. The correlation is still far from perfect, but may offer a means of inferring an averaged mean ice thickness from mean SAR backscatter under certain conditions.

3. SAR backscatter versus passive microwave brightness temperatures reveals that the X-band, single polarization SAR backscatter values (especially at the highest resolution), may not be as effective in discriminating certain ice types as originally thought. The SAR imagery has been noted for good characterization of the ice cover including visual discrimination of multiyear ice floes from first-year ice. However, the SAR backscatter, especially for multiyear ice, varies considerably and overlaps with those of the other ice types. While the variation is partly due to the inherent noise in the signal, it is only by increasing the scales to about a kilometer that a more recognizable pattern in the SAR data is observed. The use of training areas for ice classification using single channel-SAR images thus requires that the proper scale is chosen and, even then, some ambiguities remain. Better results are expected with multichannel SAR systems.

The multispectral passive microwave data, on the other hand, are useful in characterizing consolidated ice even at the finest resolution possible. The scatter plots for 18 GHz versus 37 GHz show very highly correlated signals from the consolidated ice region. However, a comparative analysis of passive microwave footprints with submarine sonar data shows a large range in the emissivity of multiyear ice and other ice types. This agrees with the analysis done previously with satellite data alone (Comiso, 1983; 1986) indicating the existence of such variations in the emissivity of multiyear ice. The effect is apparently more obvious when largely separated areas of the Arctic are examined. Three regions in the central Arctic where multiyear ice floes are

expected to be vast and easily resolved by the sensors were observed to have emissivities which are considerably different from each other. The implication for this is that the multiyear ice concentration cannot be inferred from the Arctic region with just a simple, linear mixing formulation.

The analysis of digital SAR data in conjunction with passive microwave data and submarine sonar indicate that much of the ridged ice identified from SAR can be either first-year ice or multiyear ice. Statistically, the data show that a large fraction of the ridging in the central Arctic region must have occurred before the current year. This suggests that roughness indeed is a primary reason for high SAR backscatter values. Again, the use of passive and active microwave systems in concert permits a more comprehensive interpretation of the characteristics of the ice cover to be carried out.

#### ACKNOWLEDGMENTS

The authors are grateful to the British Royal Navy, Admiralty Research Establishment, and NASA for making it possible to conduct such a unique experiment. They are especially thankful to Dr. E. Mollo-Christensen for guidance and advice during the mission and to Andrew Cowan and Jonathan Carter for logistic support. Programming and technical support were provided by a number of people including Americo Allegrino of STX, William Wang of JPL, Dr. N. Davis of Scott Polar Research Institute, and N. Flack and Miss A. Scoon of SAIC-Polar Oceans Associates. The P3 aircraft component of the mission was supported by the Ocean Processes Program of NASA. Funding support for the analysis of submarine and SAR data was provided by the Office of Naval Research order contract N00014-89-C-0016 to SAIC; and the National Environment Research Council of Great Britain.

TABLE 1. PHYSICAL CHARACTERISTICS OF VARIOUS SENSORS

Sensor	Wavelength	Polarization	Resolution	Altitude (or depth)	Swath Width
SAR	X	HH	16m	10,000	63km
			6m		17m
ESMR	19.5	H	750 by 400m	6000	14.6km
			60 by 30m	220	0.60 km
AMMR	37.0	H&V	1528 by 750m	6000m	
	21.0	V	1528 by 750m	6000m	
	18.0	H&V	1528 by 750m	6000m	
	37.0	H&V	60 by 31m	220m	
	21.0	V	60 by 31m	200m	
	18.0	H&V	60 by 31m	200m	
OL			1 by 1m	220	
T-5	11.5 $\mu$				
Sidescan Sonar			6 by 6	100 m	1.5 km
Upward looking			8 by 8m	100 m	

TABLE 2. SONAR/LIDAR STATISTICS

	Sonar			Lidar		
	1	2	3	1	2	3
Mean draft/elevation	5.092	5.146	6.173	0.757	0.711	0.607
Modal draft/elevation	2.9	2.6	2.1	0.6	0.6	0.2
Keels per km>5m deep	8.573	6.550	7.758			
mean draft m	8.986	9.489	10.471			
>9m deep	3.222	3.050	6.238			
mean draft	12.906	12.437	13.350			
Sails per km > 0.7 m high				14.51	11.18	9.54
mean height m				1.513	1.554	1.567
>1.05 m high				9.21	7.81	6.95
mean height m				1.88	1.84	1.83
Greatest draft/elevation m	27.3	26.5	25.5	5.8	4.9	4.3

## REFERENCES

- Carsey, F., Summer Arctic sea ice character from satellite microwave data, J. Geophys. Res., 90, 5015-5034, 1985.
- Cavalieri, D. J., P. Gloersen, and W. J. Campbell, Determination of sea ice parameters with the Nimbus 7 SMMR, J. Geophys. Res., 89, 5355-5369, 1985.
- Colony and Munoz, Arctic Sea Ice Buoy Data, 1987.
- Comiso, J.C., Characteristics of Arctic winter sea ice from satellite multi-spectral microwave observations, J. Geophys. Res., 91, 975-994, 1986.
- Comiso, J.C., Sea ice microwave emissivities from satellite passive microwave and infrared observations, J. Geophys. Res., 88, 7686-7704, 1983.
- Comiso, J.C., Multiyear ice classification and mass balance studies using Arctic passive microwave data, J. Geophys. Res., Accepted
- Gloersen P. and D.J. Cavalieri, Reduction of weather effects in the calculation of sea ice parameters with Nimbus 7 SMMR, J. Geophys. Res., 93, 3913-3919, 1986.
- Hall, R.T., and D.A. Rothrock, Sea ice displacement from Seasat Synthetic Aperture Radar, J. Geophys. Res., 86, 11078, 1981.
- Hibler, W.D. III, Removal of aircraft altitude variation from laser profiles of the Arctic pack ice, J. Geophys. Res., 77(36), 7190-7195, 1972.
- Hibler, W.D. III, A dynamic thermodynamic sea ice model, J. Phys. Oceanogr., 9, 815-846, 1979.
- Holt, B., J. Crawford, and F. Carsey, Characteristics of sea ice during the Arctic winter using multifrequency aircraft radar imagery, W. F. Weeks Symposium, CRREL Special Report, In Press.
- Holyer, I.J., P. Wadhams, and R.T. Lowry, Laser ice profile analysis using

- interactive graphics, Scott Polar Research Institute Tech. Rep. 77-1, Cambridge, England, 1-26, 1977.
- Krabill, W.B., J.C. Collins, L.E. Link, and M.L. Butler, Airborne laser topographic mapping results from joint NASA/U.S. Army Corps of Engineers Experiments, Photogrammetric Engineering and Remote Sensing, 50, No. 6, 685, 1984.
- Onstott, R.G., T.C. Grenfell, C. Maetzler, C.A. Luther, and E.A. Svendsen, Evolution of microwave sea ice signatures during early and mid summer in the marginal ice zone, J. Geophys. Res., 92, 6825-6837, 1987.
- Parkinson, C.L., J.C. Comiso, H.J. Zwally, D.J. Cavalieri, P. Gloersen, and W.J. Campbell, Arctic sea ice, 1973-1976: Satellite Passive Microwave Observations, NASA SP489, 296pp, 1987.
- Svendsen, E., K. Kloster, B. Farrelly, O.M. Johannessen, J.A. Johannessen, W.J. Campbell, P. Gloersen, D.J. Cavalieri, and C. Matzler, Norwegian Remote Sensing Experiment: Evaluation of the Nimbus 7 scanning multichannel microwave radiometer for sea ice research, J. Geophys. Res., 88, 2755-2769, 1983.
- Swift, C.T., L.S. Fedor, and R.O. Ramseier, An algorithm to measure sea ice concentration with microwave radiometers, J. Geophys. Res., 90, 1087-1099, 1985.
- Tucker III, W.B., A.J. Gow, W.F. Weeks, Physical properties of summer sea ice in the Fram Strait, J. Geophys. Res., 92, 6787-6804, 1987.
- Wadhams, P., Sea ice topography in the Beaufort Sea and the effect on oil containment, AIJEX Bull., Div. of Marine Resources, Univ. of Washington, Seattle, 33, 1-52, 1976.

Wadhams, P., A comparison of sonar and laser profiles along corresponding tracks in the Arctic Ocean, in Sea Ice Processes and Models, ed. by R.S. Pritchard, Univ. of Washington Press, Seattle, 283-299, 1980.

Wadhams, P. Sea ice topography of the Arctic Ocean in the region 70°W to 25°E, Phil. Trans. Roy. Soc. Lond., 302(464), 45-85, 1981.

Wadhams, P., Sea ice thickness distribution in Fram Strait, Nature, 305(5930), 108-111, 1983a.

Wadhams, P., Arctic sea ice morphology and its measurement, J. Underwater Technol., 9(2), 1-12, 1983b.

Wadhams, P., The underside of Arctic sea ice imaged by sidescan sonar, Nature, 333(6169), 161-164, 1988.

Wadhams, P., and S. Martin, Processes determining the bottom topography of multiyear Arctic sea ice, W.F. Weeks Symposium, CRREL Special Rept., In Press.

Wadhams, P., J.C. Comiso, A.M. Cowan, J. Crawford, G. Jackson, W. Krabill, R. Kutz, C.B. Sear, R. Swift, and W.B. Tucker, Concurrent remote sensing of Arctic sea ice from submarine and aircraft, Int. J. Remote Sensing, (submitted, 1989).

Zwally, H.J., J.C. Comiso, C.L. Parkinson, W.J. Campbell, F.D. Carser, and P. Gloersen, Antarctic sea ice 1973-1976 from satellite passive microwave observations, NASA Spec. Publ. 459, 224 pp., 1983.

## LIST OF FIGURES

Plate 1. A 40-km section of X-band SAR imagery from north of Greenland.

Eastbound (line A) and westbound (line B) flight lines of the P-3A aircraft are overlaid on the image, as is the footprint of the AMMR (Airborne Multichannel Microwave Radiometer). False color ESMR (Electrically Scanning Microwave Radiometer) imagery from lines A and B are also shown; the flight lines mark the center of the ESMR images which extend so as to just overlap laterally. The box outlined in red shows the location of the imagery and profile in Plate 2.

Plate 2. A 10-km section of imagery and profiles from the various sensors.

- (a) The SAR brightness levels along the track of the submarine.
- (b) The upward looking sonar profile of ice draft. (c) Sidescan sonar imagery of the ice underside, with a 1000-m swath width.
- (d) Contrast-stretch SAR imagery, with submarine and aircraft tracks overlaid. (e) The AOL laser profile of ice elevation.
- (f) PRT-5 infra-red radiometer profile. (g) Microwave brightness temperatures from the AMMR.

Figure 1. NASA P3 flight tracks as navigated by the GPS system for the May 19, May 20, and May 21, 1987 missions.

Figure 2. Comparison of relative positions determined from NASA P3 aerial photographs with those inferred from the SAR images.

Figure 3. A sidescan sonar image with the corresponding SAR image. In the center is a lead which is open on its right side and refrozen on the left side. To the left of the lead is a region of heavy



continuous ridging. To the far left is a multiyear ice floe (A) with a ridge in between. On the right of the lead is an undeformed first year ice floe.

Figure 4. Probability Distributions of (a) Ice Draft, and (b) elevation.

Figure 5. Results of a coordinate transformation in which the elevation distribution for 60 km of track is stretched along the abscissa by a factor of 7.909 (mean draft/elevation ratio) and plotted against corresponding draft distribution.

Figure 6. Distributions of keel drafts and ridge elevations.

Figure 7. Distribution of keel drafts for 60-km section of track with distribution of sail heights.

Figure 8. Cross correlation coefficients for various averaging windows for mean AOL elevation versus mean SAR backscatter, elevation standard deviation versus mean backscatter, and elevation standard deviation versus backscatter standard deviation.

Figure 9. Mean elevation and mean backscatter for the 1 km averaging window for the 120 km track.

Figure 10. Mean elevation versus mean SAR backscatter with best fit regression line for 1 km averaging window.

Figure 11. Correlation study of SAR backscatter versus Draft.

Figure 12. Scatter Plots of (a) 18 GHz versus 37 GHz, and (b) SAR vs 37 GHz at vertical polarization, over the study region, using high resolution AMMR data.

Figure 13. Ice types inferred from submarine sonar versus 37-GHz (Vertical) brightness temperature data.

Figure 14. High resolution AMMR 18-GHz vs 37-GHz data for (a) May 19, 1987 (b) May 20, 1987, and (c) May 21, 1987 covering different regions of the Arctic.

Figure 15. Scatter Plots using high altitude data: (a) AMMR 18 GHz versus 37 GHz, horizontal, b) SAR versus 37 GHz, horizontal, (c) AMMR 18 GHz versus 37 GHz, vertical, and (d) SAR versus AMMR 37 GHz, vertical.

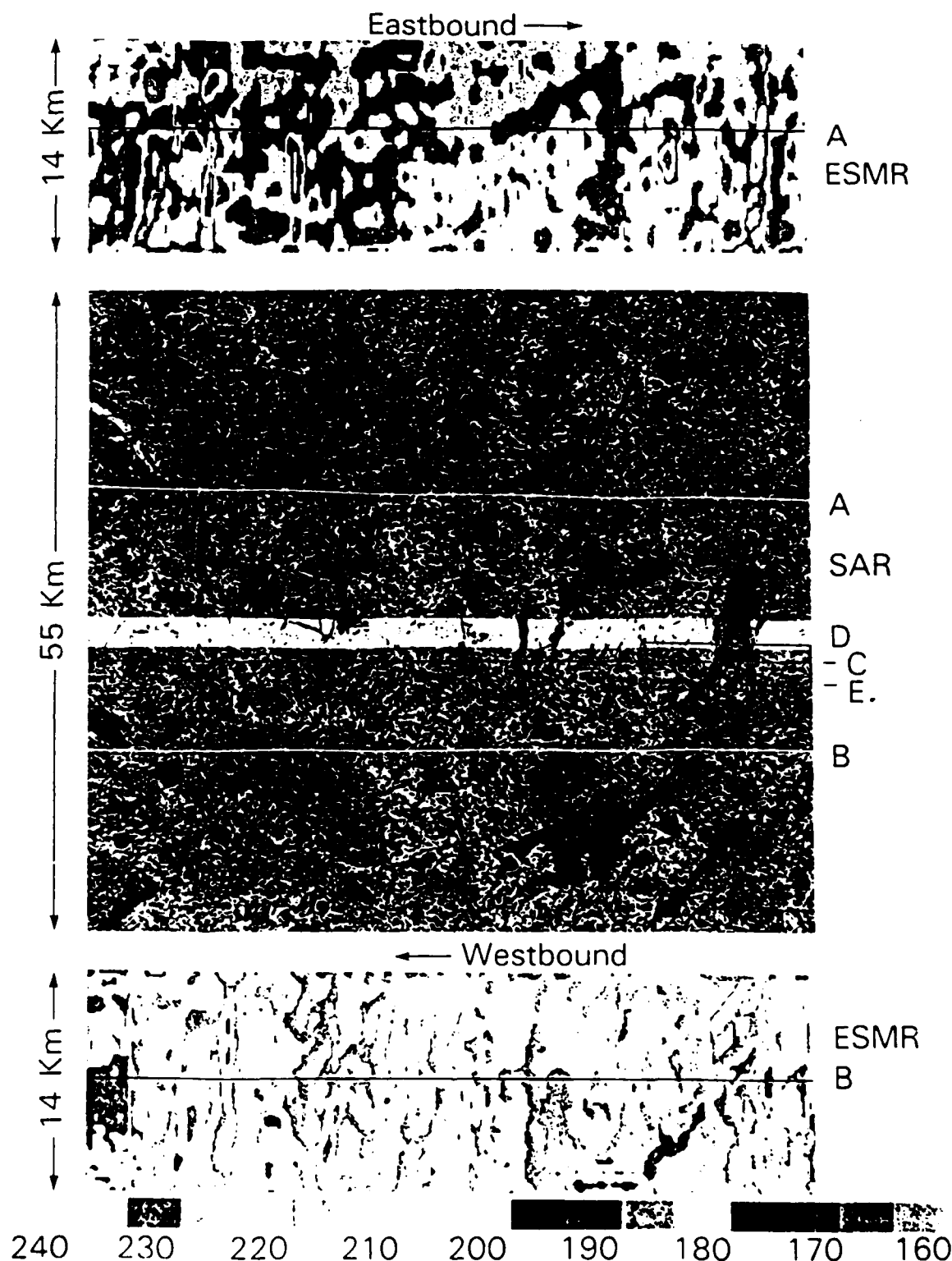


Plate 1. A 40-km section of X-band SAR imagery from north of Greenland. Eastbound (line A) and westbound (line B) flight lines of the P-3A aircraft are overlaid on the image, as is the footprint of the AMMR (Airborne Multichannel Microwave Radiometer). False color ESMR (Electrically Scanning Microwave Radiometer) imagery from lines A and B are also shown; the flight lines mark the center of the ESMR images which extend so as to just overlap laterally. The box outlined in red shows the location of the imagery and

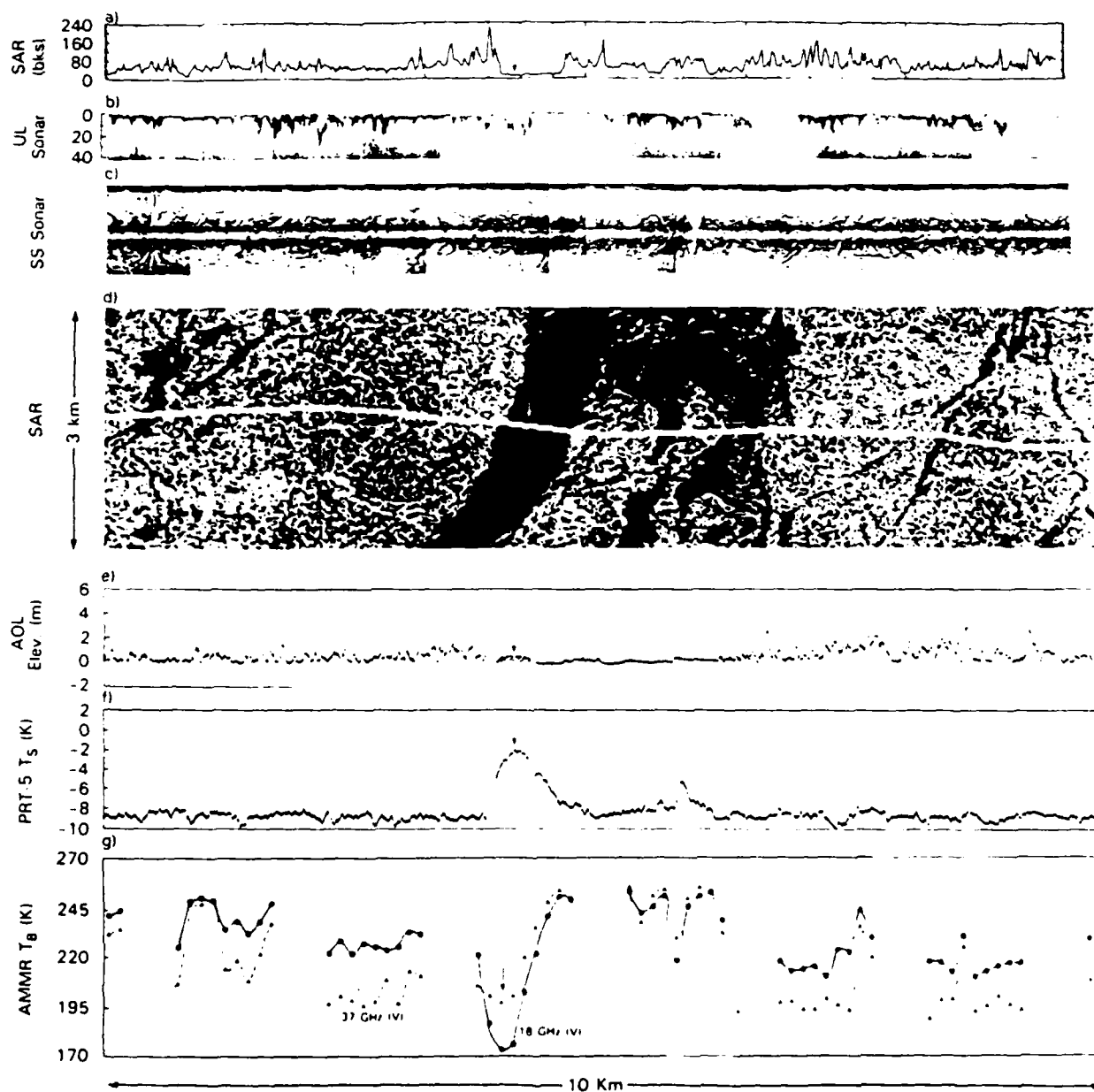


Plate 2. A 10-km section of imagery and profiles from the various sensors.  
 (a) The SAR brightness levels along the track of the submarine.  
 (b) The upward looking sonar profile of ice draft. (c) Sidescan sonar imagery of the ice underside, with a 1000-m swath width.  
 (d) Contrast-stretch SAR imagery, with submarine and aircraft tracks overlaid. (e) The AOL laser profile of ice elevation.  
 (f) PRT-5 infra-red radiometer profile. (g) Microwave brightness temperatures from the AMMR.

## NASA P-3 Flight Track

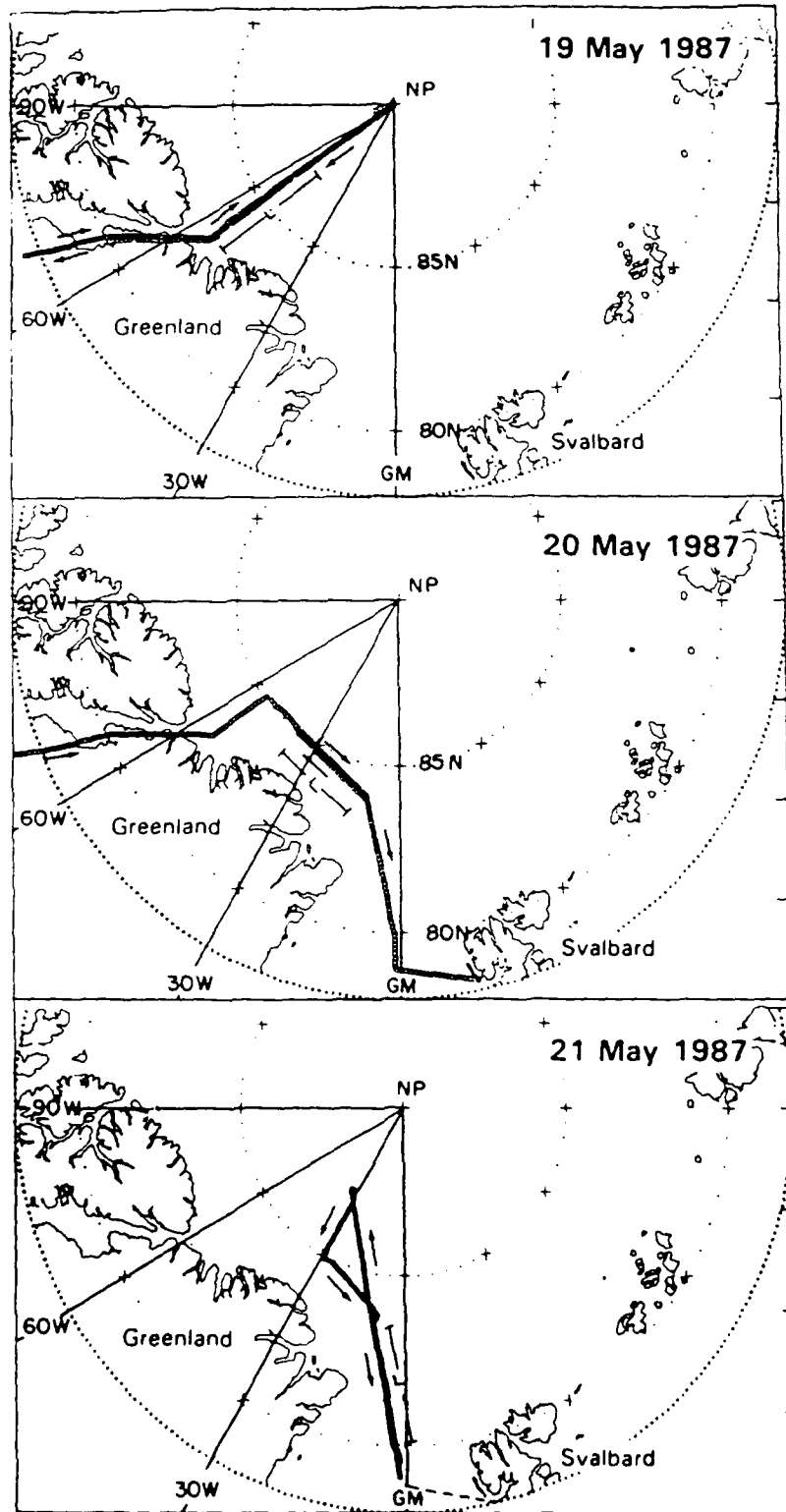


Figure 1. NASA P3 flight tracks as navigated by the GPS system for the May 19, May 20, and May 21, 1987 missions.

# High Altitude Data on May 20, 1989

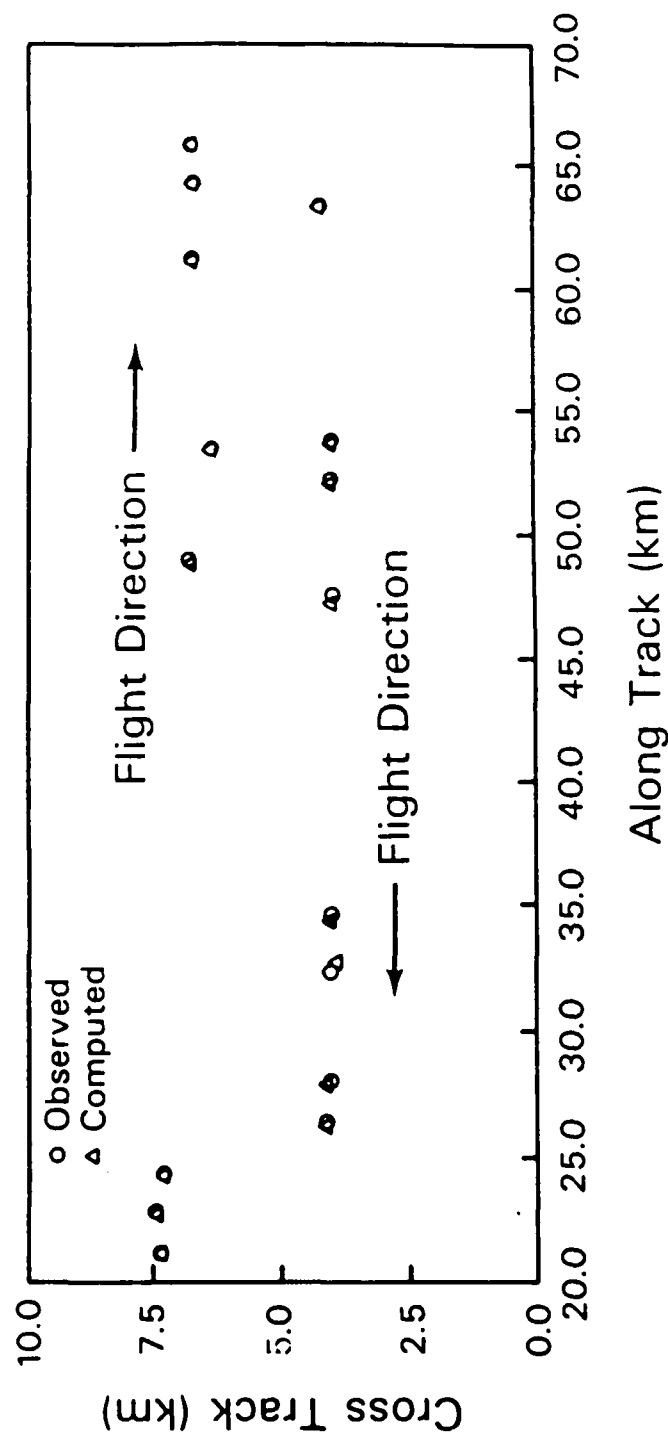


Figure 2. Comparison of relative positions determined from NASA P3 aerial photographs with those inferred from the SAR images.

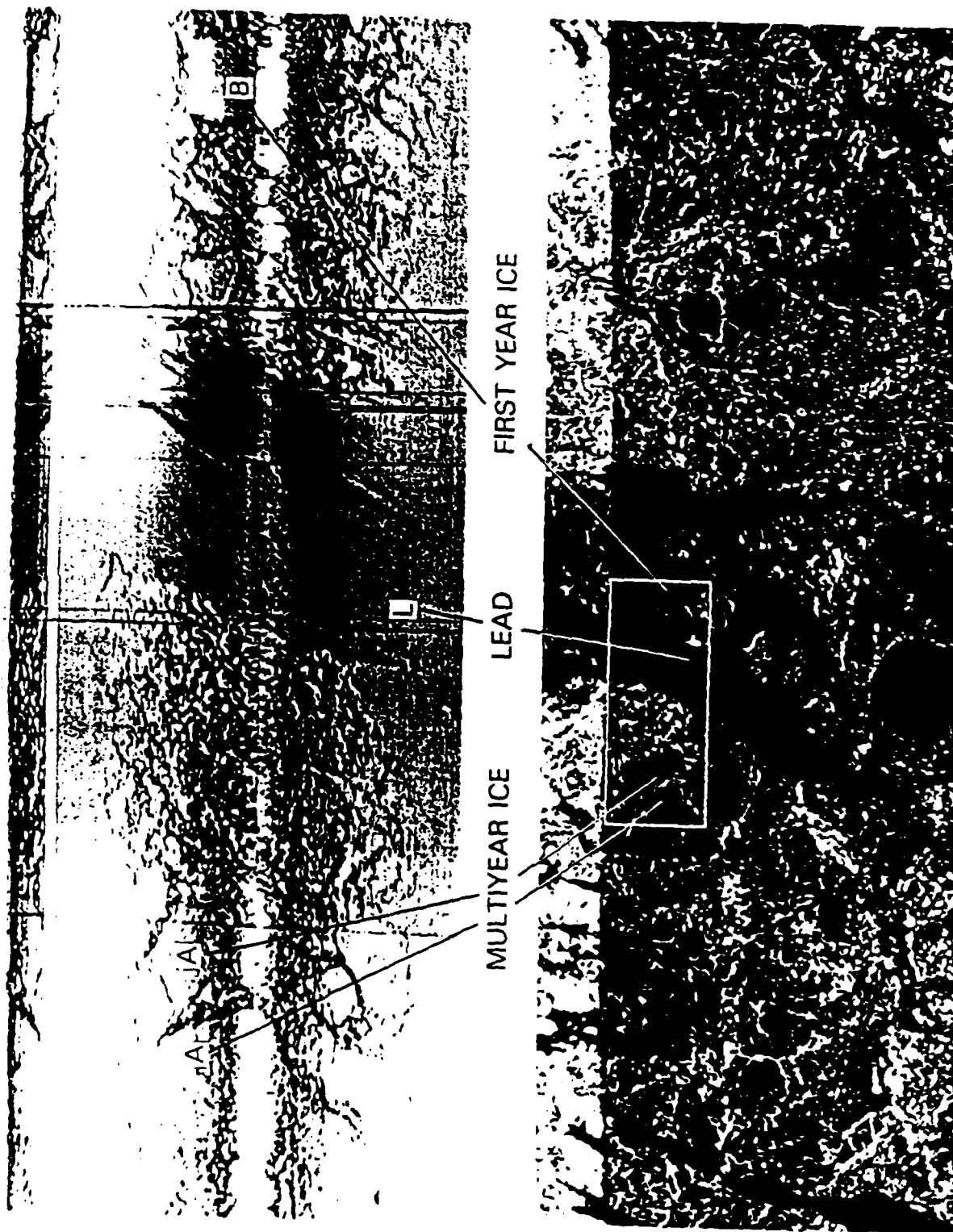


Figure 3. A side-scan sonar image with the corresponding SAR image. In the center is a lead which is open on its right side and refrozen on the left side. To the left of the lead is a region of heavy continuous ridging. To the far left is a multiyear ice floe (A) with a ridge in between. On the right of the lead is an undetermined first year ice floe.

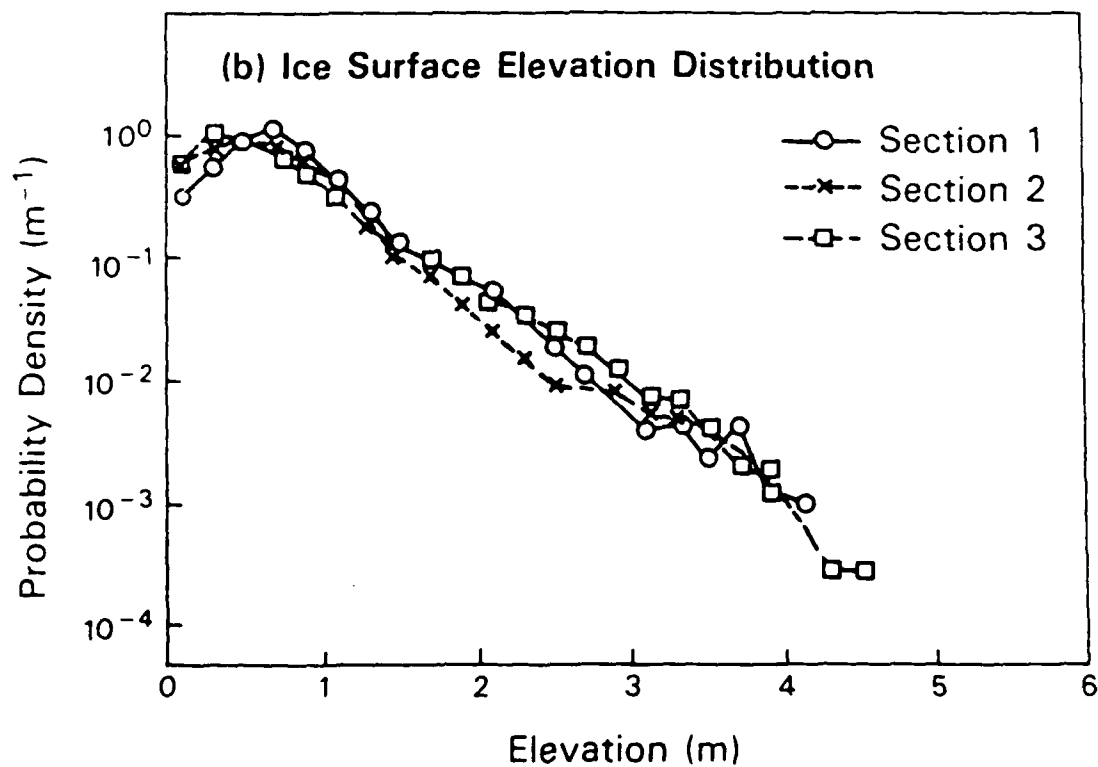
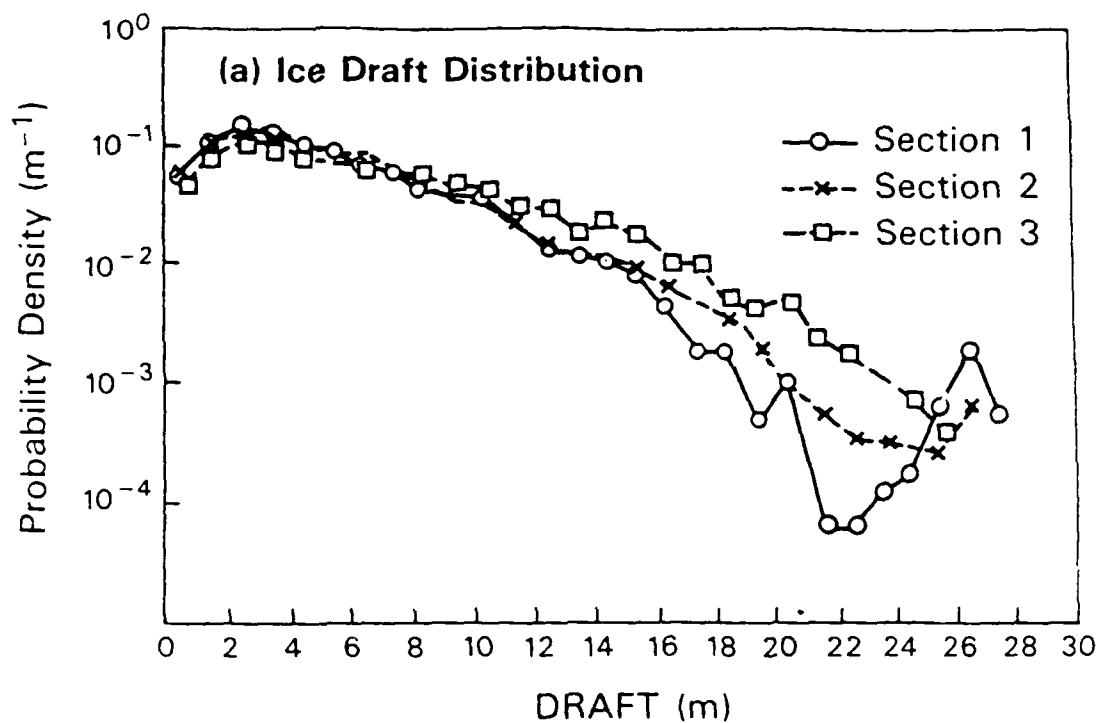


Figure 4. Probability Distributions of (a) Ice Draft, and (b) elevation.



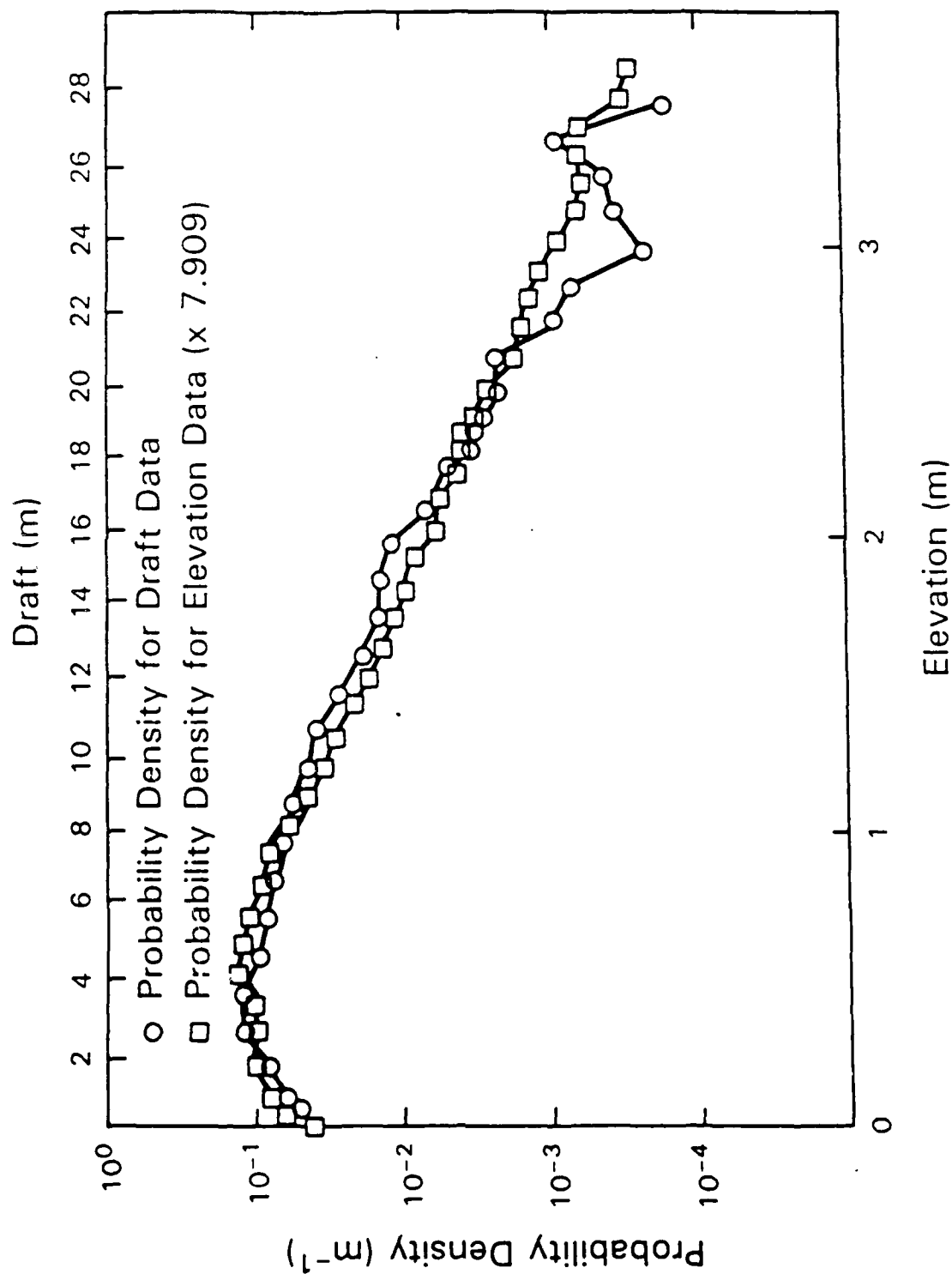


Figure 5. Results of a coordinate transformation in which the elevation distribution for 60 km of track is stretched along the abscissa by a factor of 7.909 (mean draft/elevation ratio) and plotted against corresponding draft distribution

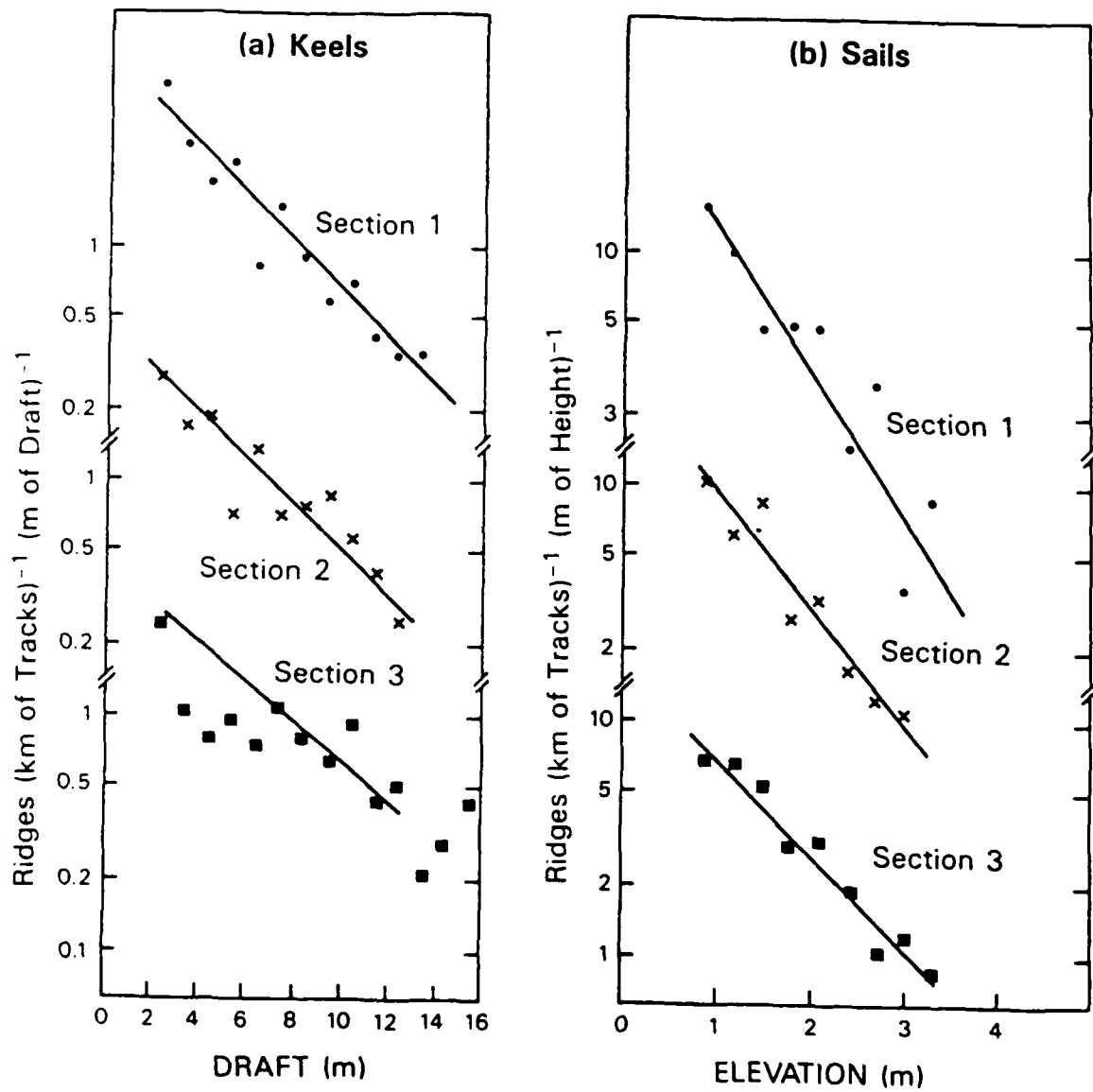


Figure 6. Distributions of keel drafts and ridge elevations.

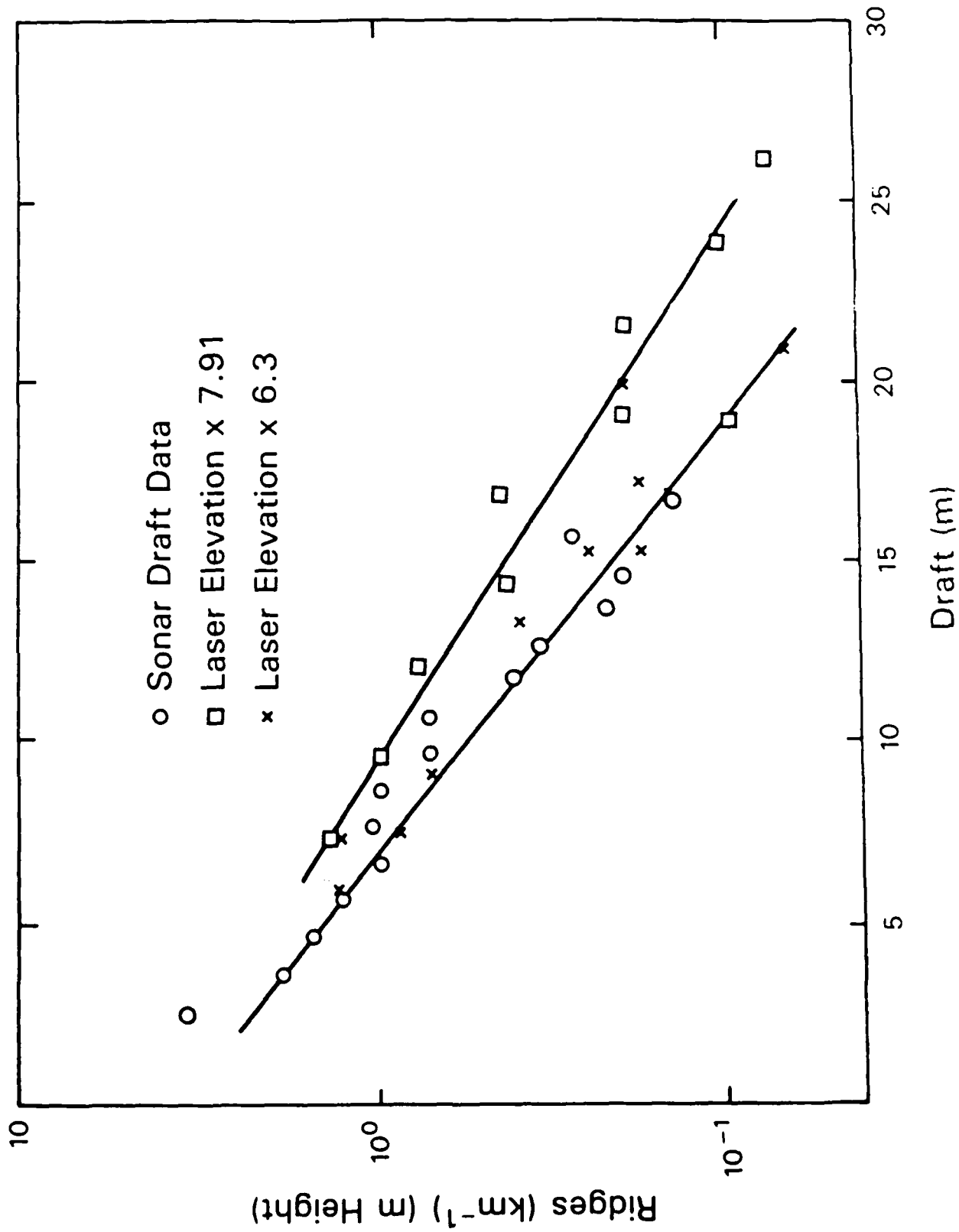


Figure 7. Distribution of keel drafts for 60-km section of track with distribution of sail heights.

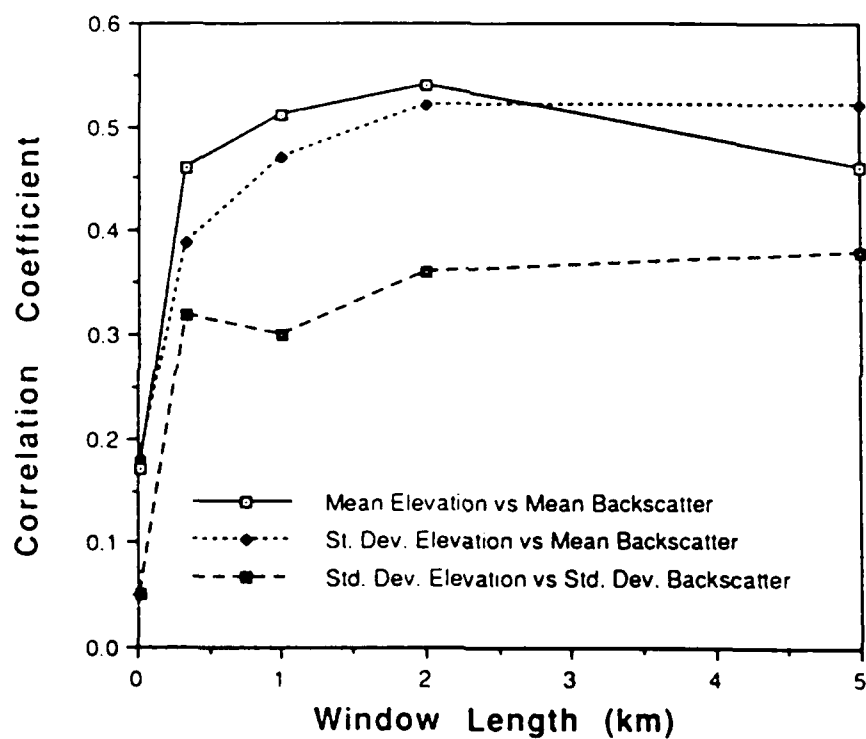


Figure 8. Cross correlation coefficients for various averaging windows for mean AOL elevation versus mean SAR backscatter, elevation standard deviation versus mean backscatter, and elevation standard deviation versus backscatter standard deviation.

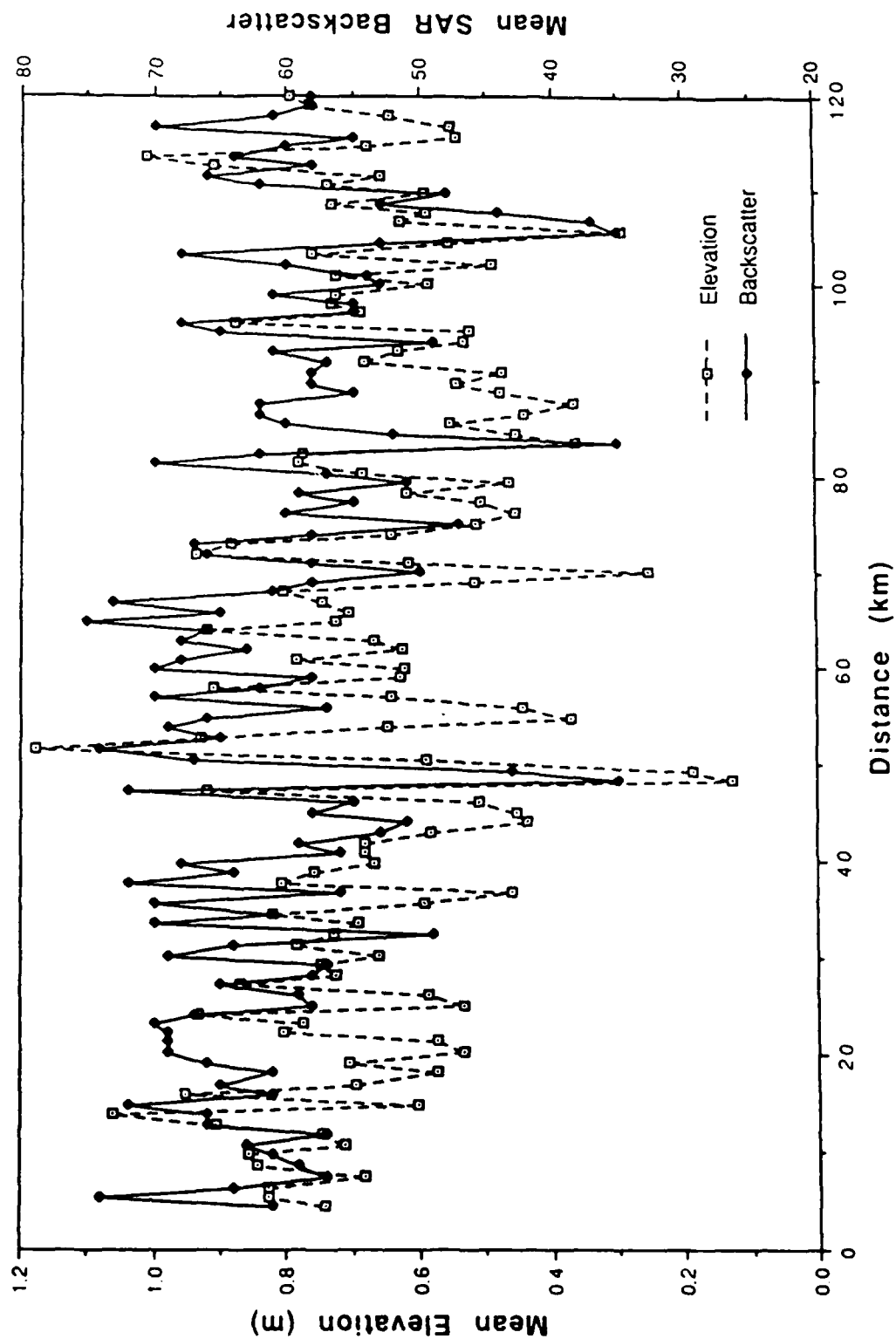


Figure 9. Mean elevation and mean backscatter for the 1 km averaging window for the 120 km track.

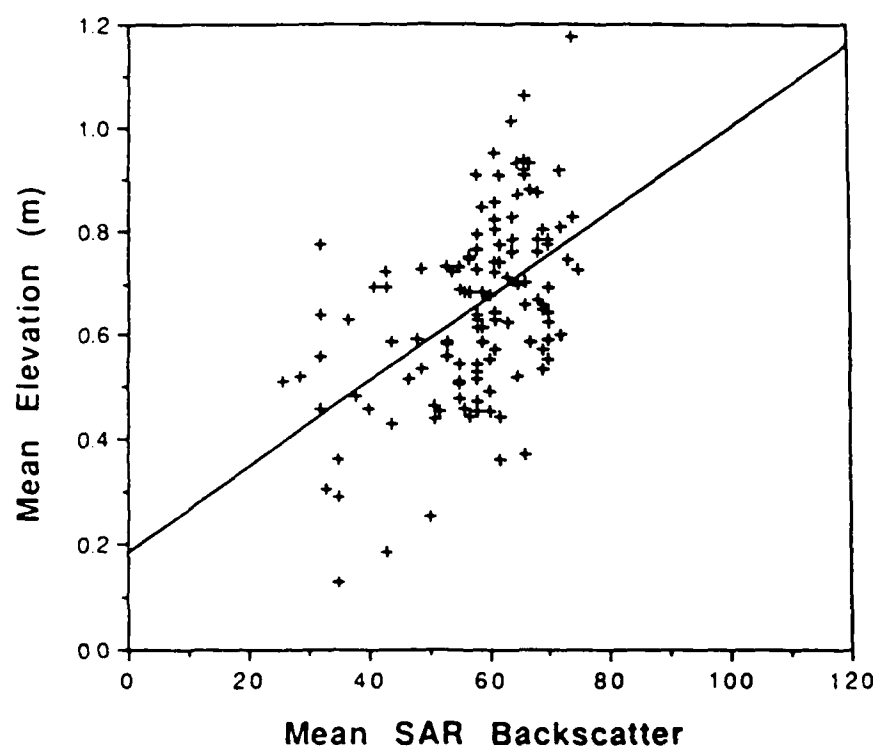


Figure 10. Mean elevation versus mean SAR backscatter with best fit regression line for 1 km averaging window.

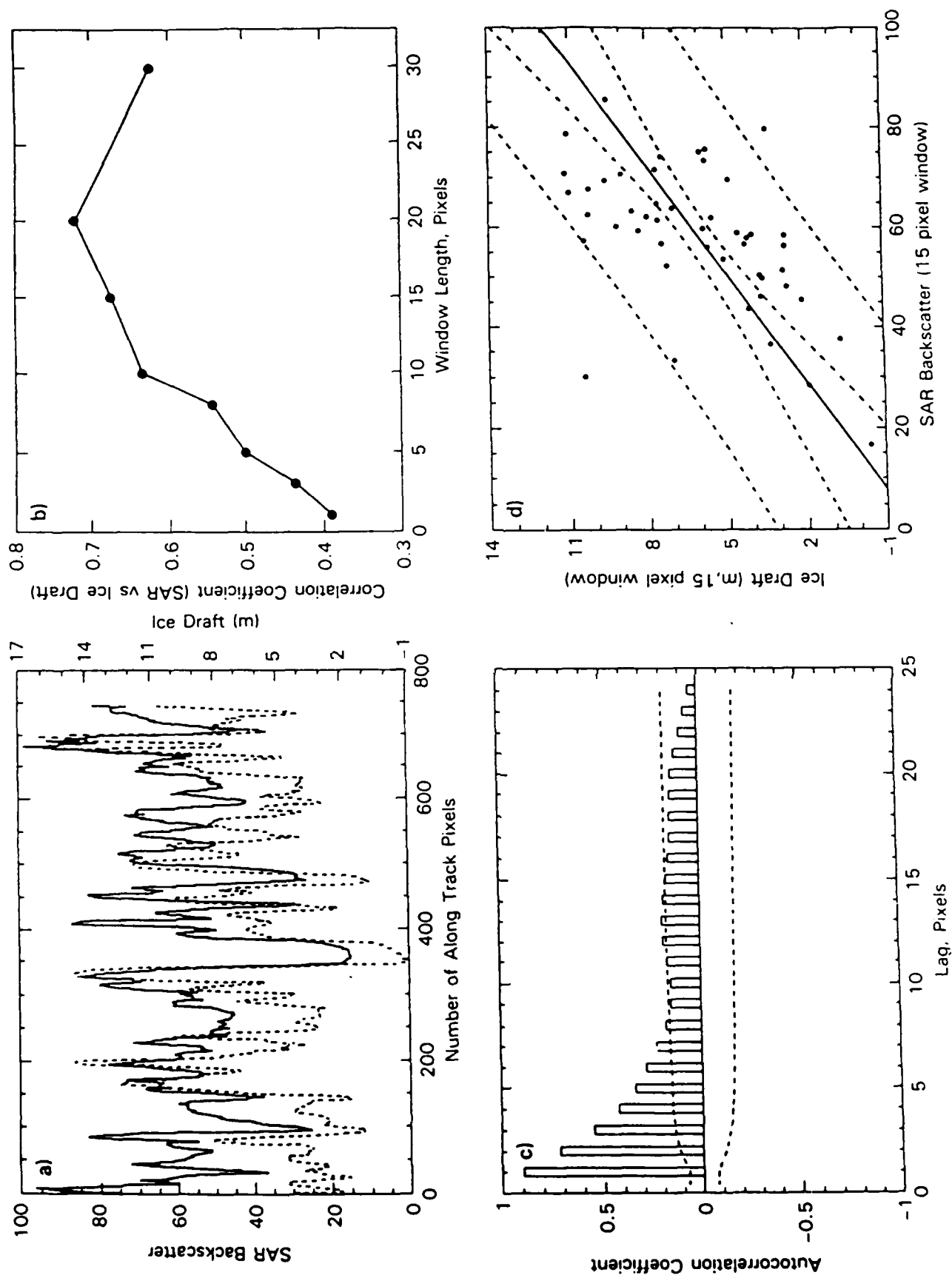


Figure 11. Correlation study of SAR backscatter versus Draft.

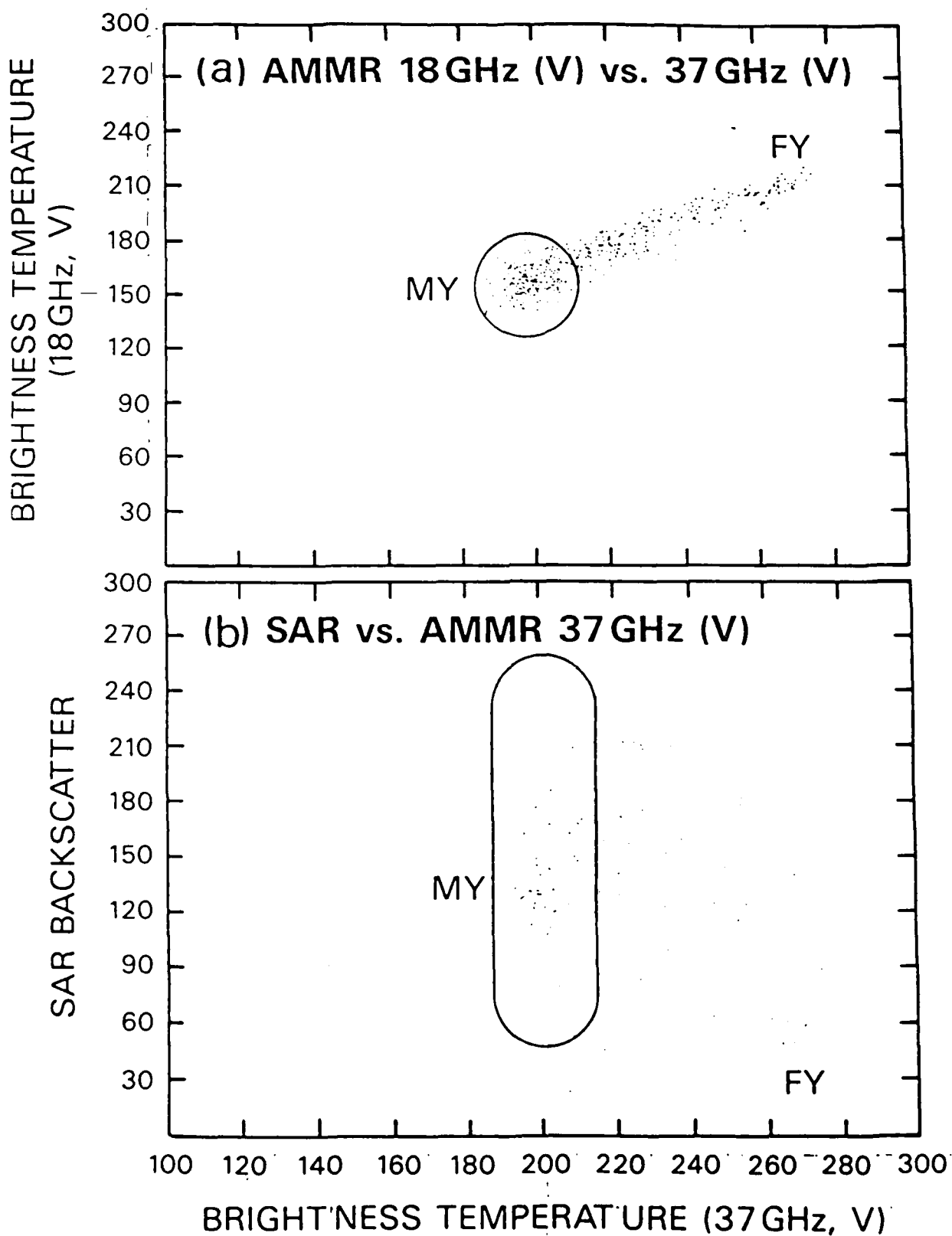


Figure 12. Scatter Plots of (a) 18 GHz versus 37 GHz, and (b) SAR vs 37 GHz at vertical polarization.



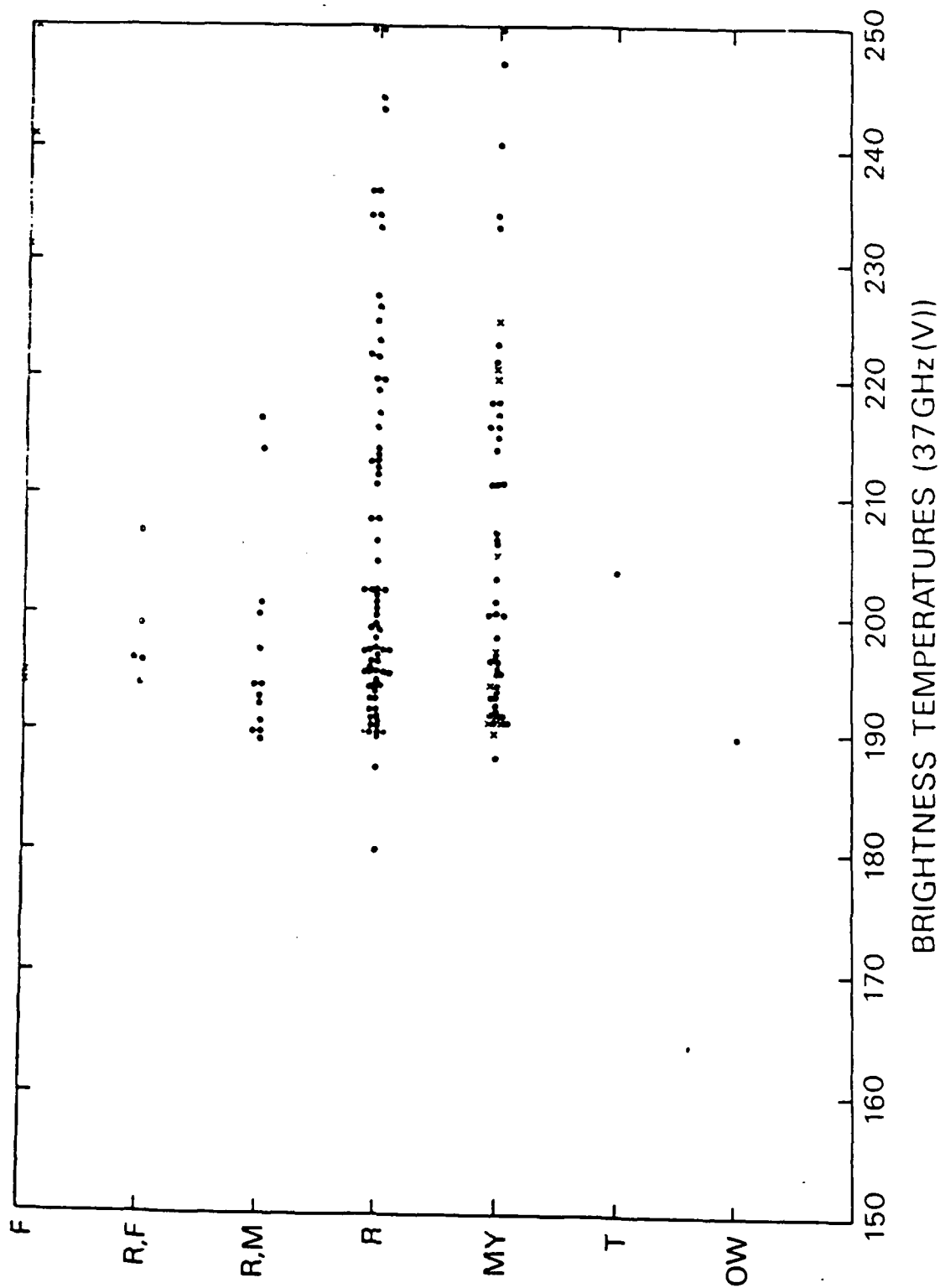


Figure 13. Ice types inferred from submarine sonar versus 37-GHz (Vertical) brightness temperature data.

# AMMR LOW ALTITUDE DATA

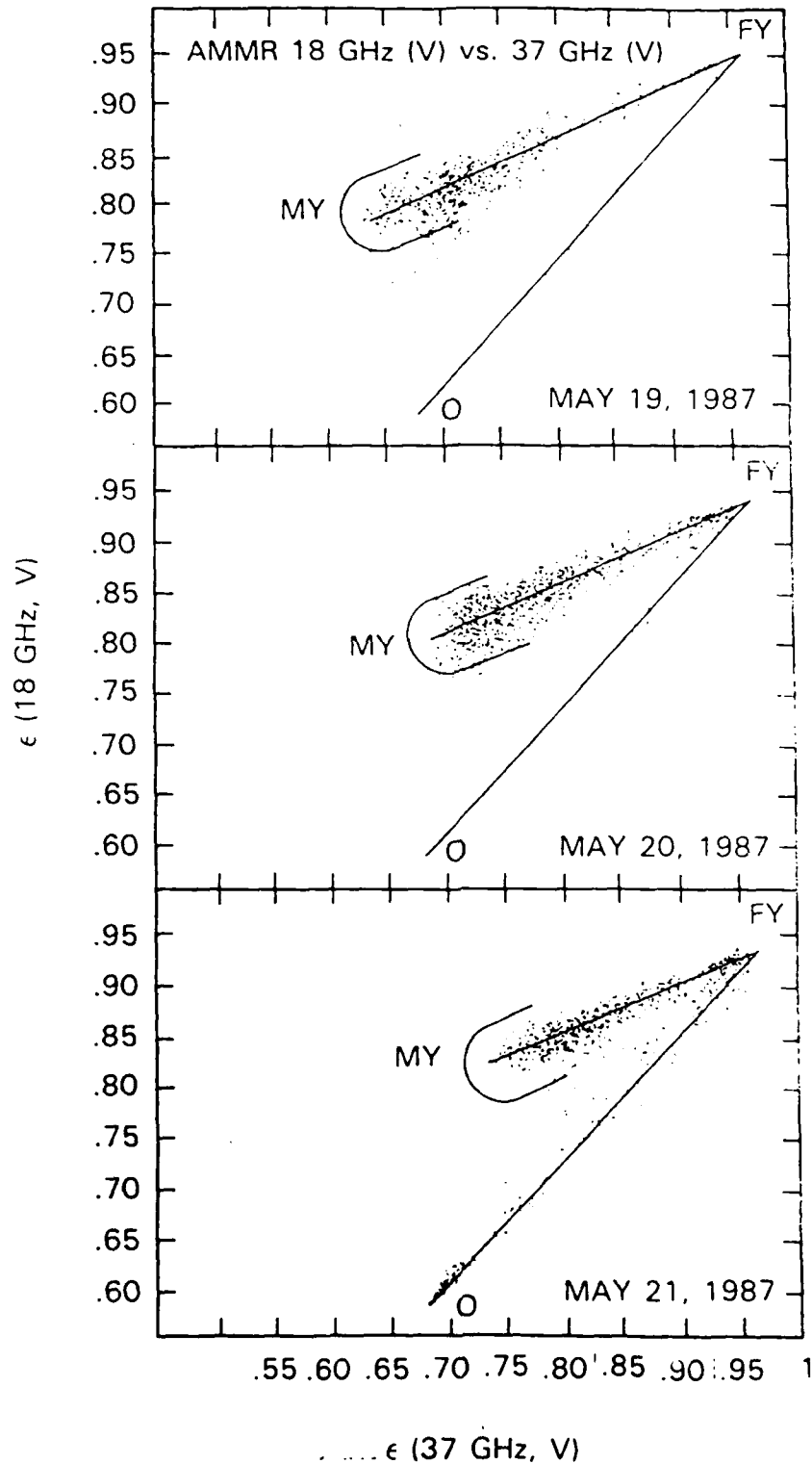


Figure 14. High resolution AMMR 18-GHz vs 37-GHz data for (a) May 19, 1987 (b) May 20, 1987, and (c) May 21, 1987 covering different regions of the Arctic.

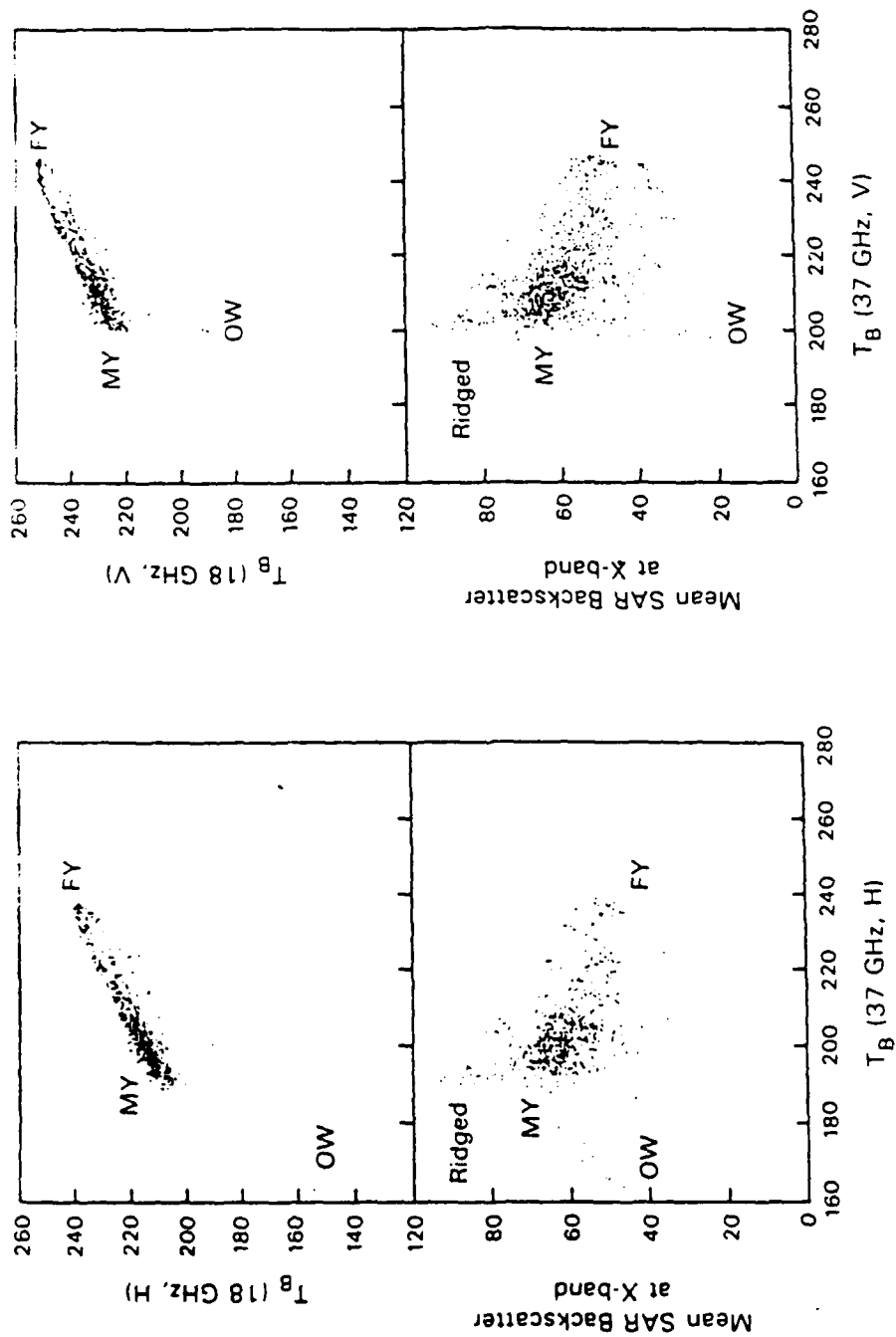


Figure 15. Scatter Plots using high altitude data: (a) AMMR 18 GHz versus 37 GHz, horizontal, (b) SAR versus 37 GHz, horizontal, (c) AMMR 18 GHz versus 37 GHz, vertical, and (d) SAR versus AMMR 37 GHz, vertical.